Oxidation pathways and emission sources of atmospheric particulate nitrate in Seoul: based on $\delta^{15}N$ and $\Delta^{17}O$ of $PM_{2.5}$

Saehee Lim[a], Meehye Lee[a,*], Joel Savarino [b], and Paolo Laj [b]

[a] Dept. of Earth and Environmental Sciences, Korea University, Seoul, 02841, South Korea

[b] Univ. Grenoble-Alpes, CNRS, IRD, Grenoble INP, Institute for Geosciences and Environmental Research (IGE), Grenoble, 38000, France

*Correspondence to: M. Lee (meehye@korea.ac.kr)

Abstract

$PM_{2.5}$ haze pollution driven by secondary inorganic NO_3^- has been a great concern in East Asia. It is, therefore, imperative to identify its sources and oxidation processes, for which nitrogen and oxygen stable isotopes are powerful tracers. Here, we determined the $\delta^{15}N$ (NO_3^-) and $\Delta^{17}O$ (NO_3^-) of $PM_{2.5}$ in Seoul during the summer of 2018 and the winter of 2018-2019, and estimated quantitatively the relative contribution of oxidation pathways for particulate NO_3^- and investigated major NO_x emission sources. In the range of $PM_{2.5}$ mass concentration from 7.5 μg m^{-3} (summer) to 139.0 μg m^{-3} (winter), the mean $\delta^{15}N$ was -0.7 ± 3.3 ‰ and 3.8 ± 3.7 ‰, and the mean $\Delta^{17}O$ was 23.2 ± 2.2 ‰ and 27.7 ± 2.2 ‰ in the summer and winter, respectively. While OH oxidation was the dominant pathway for NO_3^- during the summer (87 %), nighttime formation via N_2O_5 and NO_3 was more important (38 %) during the winter, when aerosol liquid water content (AWLC) and nitrogen oxidation ratio (NOR) were higher. Interestingly, the highest $\Delta^{17}O$ was coupled with the lowest $\delta^{15}N$ and highest NOR during the record-breaking winter $PM_{2.5}$ episodes, revealing the critical role of photochemical oxidation process in severe winter haze development. For NOx sources, atmospheric $\delta^{15}N$ (NO_x) estimated from measured $\delta^{15}N$ (NO_3^-) considering isotope fractionation effects indicates vehicle emissions as the most important emission source of NO_x in Seoul. The contribution from biogenic soil and coal combustion was slightly increased in summer and winter, respectively. Our results built on multiple-isotope approach provide the first explicit evidence for NO_3^- formation processes and major NO_x emission sources in Seoul

megacity and suggest an effective mitigation measure to improve $PM_{2.5}$ pollutions.

Keywords: nitrate, NO_x, oxidation processes, emission sources, $PM_{2.5}$ haze, triple oxygen isotope, nitrogen stable isotope

1. Introduction

In Northeast Asia, air pollution characterized by high $PM_{2.5}$ (particulate matters with aerodynamic diameter smaller than 2.5 μm) and ozone concentrations has received significant attention due to its serious effects on human health (Lelieveld et al., 2015; Xie et al., 2019). As a result of extensive efforts by East Asian countries to improve the ambient air quality, anthropogenic emissions of SO_x, NO_x, and CO has been significantly reduced, particularly in China (Cheng et al., 2019). Nonetheless, the number of severe haze events and the duration have been increased, which is not understood clearly.

It is also noteworthy that there are common chemical and meteorological characteristics in the occurrence of the $PM_{2.5}$ haze pollution in northeast Asia, such as inorganic species-dominated chemical composition (Liu et al., 2018; Shao et al., 2018; Wang et al., 2019a) and transboundary transport of haze aerosol depending on the synoptic atmospheric circulation (Quan et al., 2020; Shi et al., 2020; Zheng et al., 2019). Overall, approximately 40% of $PM_{2.5}$ consists of NO_3^-, SO_4^{2-}, and NH_4^+ (secondary inorganic aerosol, "SIA") in both urban and background sites in China (Liu et al., 2018) for the period of 2012-2013. The mass contribution of SIA was further augmented up to 69% at urban Beijing and island sites (Changdao) in North China Plain ("NCP") during the 2016 spring (Lim et al., 2020). A large increase in SIA mass is particularly associated with efficient formation of NO_3^- in cold months (most frequently in Dec. to Mar.), leading to a rapid increase in $PM_{2.5}$ concentration and developing a persistent haze pollution on a regional scale (Li et al., 2018; Xu et al., 2019). Recent studies suggest that the regional occurrence of the $PM_{2.5}$ haze events derived by NO_3^- across Asian continent has been associated with long-range transport of air pollutants promoted by cold fronts and their intrusion in downward regions by the development of the atmospheric boundary layer (Kang et al., 2019; Lee et al., 2019). However, scientific understanding is still limited because the rapid increase of $PM_{2.5}$ NO_3^- is the result of complex interplay of oxidation and transformation mechanisms producing NO_3^- from various fossil and non-fossil sources of NO_x with micro-to-synoptic meteorology creating the conditions for NO_3^- formation. In addition, considering that NO_x emissions from bottom-up emission inventory are

smaller than top-down estimates by satellites (e.g.,Goldberg et al., 2019), our understanding of NO_x emissions is poor.

In order to better understand processes of NO_3^- formation including NO_x emission sources in East Asia, a growing number of recent studies have suggested nitrogen and oxygen stable isotope-based measurement as a robust and useful tool for providing important clues for NO_3^- formation as well as NO_x emission sources (He et al., 2018; Lim et al., 2019, 2020; Song et al., 2019; Zong et al., 2017, 2020). The isotopic composition is expressed in parts per thousand (‰) and reported as δ (‰) $=(R_{sample}/R_{standard}-1) \times 1000$ with R being the ratio of the heavy isotope over the light isotope (e.g., $^{15}N/^{14}N$, $^{18}O/^{16}O$, $^{17}O/^{16}O$) in a sample (R_{sample}) and in the international standard ($R_{standard}$). The international standards are the Vienna Standard Mean Ocean Water, VSMOW and atmospheric N_2 for oxygen and nitrogen ratios, respectively. In terms of NO_x emission sources, the major NO_x sources are distinguished in their nitrogen isotopic compositions; biogenic soil (driven by fertilizer use; -35.1‰ ± 10.2‰) (Felix and Elliott, 2014; Li and Wang, 2008; Yu and Elliott, 2017), biomass burning (1.8‰ ±1.8‰) (Fibiger and Hastings, 2016), vehicle emissions (-2.5‰ ± 1.5‰) (Walters et al., 2015), and coal combustion (14.2‰ ± 4.5‰) (Felix et al., 2012; Heaton, 1990). Despite evidences that $\delta^{15}N$ (NO_x) can serve as a useful tracer of NO_x emission sources, during NO_y photochemical cycling and its loss processes, the $\delta^{15}N$ of initial NO_x can be significantly altered by both kinetic and equilibrium isotopic fractionation effects (ε_N), complicating the link between $\delta^{15}N$ (NO_3^-) and $\delta^{15}N$ (NO_x) (Freyer et al., 1993; Li et al., 2020).

The formation processes of HNO_3 in the atmosphere consist of NO-NO_2 photochemical cycle (R1-R3) and post NO_2 oxidation reactions (R4-R8). During the NO_x cycling, nitrogen isotopic fractionation is affected by unidirectional reactions of Leighton cycle and NO_x isotope exchange equilibrium. A recent laboratory experiment has shown that the Leighton cycle isotope effect (LCIE) associated solely with O_3 reaction (R1) and equilibrium isotopic effect (EIE) were -10 ‰ and 28.9 ‰ at room temperature, respectively (Li et al., 2020). The relative importance of these two effects on $\delta^{15}N$ (NO_2) also depends on NO_x levels, leading to increase (decrease) in $\delta^{15}N$ (NO_2) relative to $\delta^{15}N$ (NO_x) values at high (low) NO_x conditions (Kamezaki et al., 2019; Li et al., 2020; Walters et al., 2018). Overall, the nitrogen isotope exchange equilibrium has been suggested to be the dominant fractionation process in NO-NO_2 cycling at urban atmosphere (Freyer et al., 1993) and oxidation reactions forming nitric acid (HNO_3) and particulate NO_3^- (Savarino et al., 2013).

$NO + O_3 \rightarrow NO_2 + O_2$ (R1)

$NO + RO_2 (HO_2) \rightarrow NO_2 + RO (OH)$ (R2)

$NO_2 + h\nu \rightarrow NO + O(^3P)$ (R3)

$NO_2 + OH \rightarrow HNO_3$ (g) (R4)

$NO_2 + O_3 \rightarrow NO_3 + O_2$ (R5)

$NO_2 + NO_3 + M \leftrightarrow N_2O_5$ (R6)

$N_2O_5 + H_2O \xrightarrow{aerosol} 2HNO_3$ (aq) (R7)

$NO_3 + RH \rightarrow HNO_3$ (g) + R (R8)

The kinetic fractionation effect during daytime oxidation of NO_2 to HNO_3 (R4) is relatively minor, being estimated to be -3‰ (Freyer, 1991). During the nighttime when most NO is oxidized to NO_2 without NO_x photolysis, the isotopic equilibrium between NO_2, NO_3, and N_2O_5 should be achieved (R6). The nighttime thermal equilibrium likely favors the partitioning of ^{15}N into N_2O_5 relative to NO_2 and consequently induces a large isotopic fractionation effect of 25.5‰ (Walters and Michalski, 2015, R5-R6). On the other hand, the nitrogen partitioning between NO_2 and NO_3 (R5) may induces a fractionation effect of about -18‰ (Walters and Michalski, 2015). These N isotope fractionation effects should be first evaluated to explore NO_x source contributions, which should be based on combining with a robust tracer for the contributions of NO_3^- oxidation pathways.

Lately, $\Delta^{17}O$ (NO_3^-) has been used for tracing NO_3^- oxidation pathways (Alexander et al., 2009, 2020; Morin et al., 2009; Savarino et al., 2007, 2013). Earlier researches observed atmospheric NO_3^- is anomalously enriched in ^{17}O (Michalski et al., 2003), which stems from O_3 formation reactions, where a rare isotope effect leads to excess ^{17}O enrichment relative to what is expected based on the ^{18}O enrichments (Thiemens, 1999, 2006)(Thiemens, 2006). This enrichment is quantified by $\Delta^{17}O$ notation (^{17}O-excess, defined as $\delta^{17}O - 0.52 \times \delta^{18}O$). Since non-zero $\Delta^{17}O$ strictly reflects a photochemical effect, NO_3^- produced by denitrification in soils should have $\Delta^{17}O$ of zero. The mass-independent $\Delta^{17}O$ signature of O_3 is transferred to NO_x, in which the number of oxygen atom from O_3 is involved in NO_x. In this way, the $\Delta^{17}O$ (NO_3^-) is served as a conservative marker to track the chemical formation of atmospheric NO_3^-. Photochemical formation by peroxy radicals (HO_2 and RO_2) leads to a relatively low $\Delta^{17}O$ (NO_3^-), whereas nighttime formation through N_2O_5 and NO_3 results in high $\Delta^{17}O$ (Michalski et al., 2003; Morin et al., 2009; Savarino et al., 2007). Consequently, the difference in $\Delta^{17}O$ (NO_3^-) suggests approaching a proportional contribution of daytime and nighttime oxidation of NO_3^-.

To date, few field studies have coupled $\Delta^{17}O$ (NO_3^-) and $\delta^{15}N$ (NO_3^-) to investigate NO_x-to-NO_3^- oxidation processes and emission sources of NO_x, e.g., field researches in Japan (Nelson et al., 2018), west Virginia USA (Rose et al., 2019), Shanghai , China (He et al., 2020) and Beijing, China (He et al., 2018; Song et al., 2020).

In this study, we present the measurement results of $\delta^{15}N$ and $\Delta^{17}O$ of NO_3^- in Seoul during the summer of 2018 and the winter of 2018-2019, when we encountered the record-breaking $PM_{2.5}$ concentrations. Then, the $\delta^{15}N$ and $\Delta^{17}O$ measurements are used to evaluate seasonally distinct atmospheric oxidation pathways of NO_3^- and to explore major NO_x source contributions in the study region.

2. Measurements and methods

2.1. Sampling

We collected $PM_{2.5}$ filter samples on the rooftop of six-story Asan science building at Korea University campus located in northeast Seoul, the capital of South Korea (37.59° N, 127.02° E; Figure 1) during the summer 2018 (26 May to 22 Aug.; n = 13) and the winter 2018-2019 (27 Dec. to 8 Mar.; n = 18). Seoul is a metropolitan area with a population of 9.77 million and known to be influenced by heavy road traffic all around. The $PM_{2.5}$ particulates were collected on quartz filters (20 cm x 25 cm ; Pallflex Products, Putnam, USA) at a nominal flow rate of 96 m^3 hr^{-1} for 1 to 3 days using a high-volume air sampler (3000 series, Ecotech, Australia). Filters were analyzed for water-soluble ions, carbonaceous compounds, total nitrogen (TN) and carbon (TC), and stable nitrogen and oxygen isotopic ratios. Reactive gases including O_3, NO, NO_2, SO_2, and CO, and meteorological suite including air temperature, relative humidity, and wind speed and direction were measured hourly at the campus and nearby monitoring sites run by the National Institute of Environmental Research (NIER) and the Korea Meteorological Administration (KAM), respectively. These data were averaged daily for comparison with filter-based chemical composition data, if necessary.

2.2. Chemical analyses

Filters were stored in a freezer pending chemical analysis. Chemical composition of $PM_{2.5}$ was determined for 8 water-soluble ions (Cl^-, NO_3^-, SO_4^{2-}, Na^+, NH_4^+, K^+, Ca^{2+}, and Mg^{2+}) by ion chromatography (IC; Eco-IC, Metrohm, Switzerland); OC and EC by an OC-EC analyzer (Sunset

Laboratory Inc., US) using the thermo-optical transmittance method (NIOSH870); and TC and total nitrogen (TN) by an elemental analyzer (EA, Fisons NA-1500NC, Thermo, Waltham, MA, USA). Mass concentrations of these constituents were corrected for laboratory and field blanks. The detection limit, determined as three standard deviations (SD) above blank concentrations, was <0.1 ppm for ionic species, 0.5 μg cm^{-3} for TC (the sum of OC and EC), and 0.8g μgN and 0.5 μgC per punched filter area for TN and TC, respectively. Details of the analytical methods can be found elsewhere (Lim et al., 2020).

Following the bacterial denitrifier method (Casciotti et al., 2002; McIlvin and Casciotti, 2011), the $\Delta^{17}O$ of NO_3^- was measured simultaneously with $\delta^{18}O$ and $\delta^{15}N$ coupled with an IRMS measurement using an in-house peripheral system at the Université Grenoble Alpes (Morin et al., 2009). In brief, NO_3^- of samples was converted to N_2O via bacterial denitrification and the N_2O was further converted into O_2 and N_2, which were separated via a gas chromatography column before being introduced to the IRMS system (Thermo Finnigan MAT 253 Isotope Ratio Mass Spectrometer). Samples were measured in batch with reference materials following strictly the identical treatment principles, including the same water matrix for standards and samples. Together with samples, a subset of international nitrate reference materials (US Geological Survey 32, 34, and 35, as well as their mixtures) was measured for correction and calibration of $\Delta^{17}O$ and $\delta^{18}O$ values relative to VSMOW and $\delta^{15}N$ values relative to air N_2. The overall accuracy of the method is estimated as the reduced standard deviation of the residuals from the linear regression between the measured reference materials and their expected values (Morin et al., 2009). For these sets of analyses, the obtained uncertainties values (1σ) were 0.4 ‰ and 0.3 ‰ for $\Delta^{17}O$ (NO_3^-) and $\delta^{15}N$ (NO_3^-), respectively. The analytical procedure used in this study strictly followed the method described in Morin et al. (2009) which adheres to the now standard bacterial method coupled with the gold catalyst for the thermal decomposition of N_2O into N_2 and O_2 (Kaiser et al., 2007).

2.3. Quantifying isotope fractionation effects

2.3.1. Isotope fractionation effects of NO_2 oxidation to atmospheric particulate NO_3^- : $\delta^{15}N$ (NO_3^-)

The HNO_3 forms through three major pathways including (i) OH pathway, (ii) O_3 pathway associated with N_2O_5, and (iii) O_3 pathway associated with NO_3.

OH pathway

When NO and NO_2 coexist in similar quantities due to the Leighton cycle, ^{15}N is preferentially partitioned into NO_2 via the equilibrium isotope effect, leading to higher $\delta^{15}N$ in NO_2 relative to NO and NO_x (Freyer et al., 1993; Walters et al., 2016). Considering the comparable concentrations of NO and NO_2 over a year in Seoul (Figure S1 and S1), the N isotope effects on $\delta^{15}N$ (NO_3^-) should be significantly affected by NO_x photochemical interactions. The relative importance of EIE and LCIE to $\delta^{15}N(NO_2)$ can be assessed by comparing lifetimes of NO_2 with respect to isotope exchange with NO ($\tau_{exchange}$) and photolysis (τ_{NO2+hv}). In this regard, the "A" factor was defined as $\tau_{exchange}/\tau_{NO2+hv} = j_{NO2}/k_1 \times [NO]$ (k_1= 8.14 × 10^{-14} cm^3 s^{-1}, Sharma et al., 1970) by Li et al. (2020, 2021). These studies demonstrated that A was as small as 0.01-0.5 in EIE-dominated regime with NO_x > 20 ppbv and the ratio of NO_2/NO_x <0.6. In Seoul, to simply evaluate the relative importance of EIE and LCIE only (not for ^{15}N correction), A factor was estimated to be 0.08 ± 0.20 (median ± standard deviation) and 0.60 ± 0.51 during the winter and summer months, respectively, indicating the significant influence of the equilibrium isotope effect on NO-NO_2 isotopic fractionation. The time series j_{NO2} was calculated using the Master Chemical Mechanisms (MCM) (Saunders et al., 2003) model.

After photochemical NO_x photochemical cycling, NO_2 is oxidized by the reaction with OH radical to form atmospheric HNO_3 ("HNO_3 (R4) pathway"). The N fractionation effect of particulate NO_3^- produced via HNO_3 (R4) pathway (ε_1, unit in ‰) can be expressed as the following, neglecting kinetic isotope effects associated with HNO_3 (R4) pathway (Walters and Michalski, 2016):

$$\delta^{15}N\ (HNO_3)\ (R4) = \delta^{15}N\ (NO_2) = \delta^{15}N\ (NO_x) + \varepsilon_1 \quad \text{(Eq. 1-1)}$$

$$\varepsilon_1 = (({}^{15}\alpha_{NO2/NO} - 1)\ (1 - f_{NO2}))/\ ((1 - f_{NO2}) + ({}^{15}\alpha_{NO2/NO} \times f_{NO2})) \quad \text{(Eq. 1-2)}$$

, where f_{NO2} is the fraction of NO_2 relative to the total NO_x, and $^{15}\alpha_{NO2/NO}$ is the temperature-dependent isotope equilibrium exchange fractionation factor for NO_2/NO (Walters et al., 2016). In the present study, the measured f_{NO2} was used individually for summer samples and a seasonal mean f_{NO2} (0.69) was applied to winter samples due to the lack of availability of continuous NO-NO_2 measurement data.

Oxidation of NO_x to HNO_3 is regarded as the formation pathway of particulate NO_3^- via the "HNO_3 (R4) pathway" due to the unconstrained isotope fractionation effect between HNO_3 and NO_3^-, resulting in the following equation:

$\delta^{15}N\ (HNO_3)\ (R4) = \delta^{15}N\ (NO_3^-)\ (R4)$ (Eq. 1-3)

O_3 pathways associated with N_2O_5, and NO_3.

During the nighttime when NO is oxidized into NO_2 without photolyzing back to NO and fresh emissions of NO is negligible, NO_x exists almost as NO_2 and thus, $\delta^{15}N\ (NO_2)$ should be reflective of the $\delta^{15}N$ of NO_x sources. If NO_2 is oxidized to N_2O_5, the isotopic equilibrium is likely to be achieved between NO_2, NO_3, and N_2O_5 by chemical equilibrium (R6) and the $\delta^{15}N$ values of N_2O_5 and NO_3 will reflect the isotope equilibrium fractionation factors relative to NO_2 (i.e., $^{15}\alpha_{N2O5/NO2}$ and $^{15}\alpha_{NO3/NO2}$, values were adopted from supplementary Table S5 in Walters and Michalski, 2016). Finally, $\delta^{15}N$ of particulate NO_3^- produced from dark pathways can be expressed as the following, neglecting currently unconstrained kinetic isotopic fractionation associated with R7 and R8 (Walters and Michalski, 2016).

$\delta^{15}N\ (HNO_3)\ (R7) = \delta^{15}N\ (N_2O_5) = \delta^{15}N\ (NO_2) + \varepsilon_2$ (Eq. 2-1)

$\varepsilon_2 = (^{15}\alpha_{N2O5/NO2} - 1)$ (Eq. 2-2)

$\delta^{15}N\ (HNO_3)\ (R7) = \delta^{15}N\ (NO_3^-)\ (R7)$ (Eq. 2-3)

$\delta^{15}N\ (HNO_3)\ (R8) = \delta^{15}N\ (NO_3) = \delta^{15}N\ (NO_2) + \varepsilon_3$ (Eq. 3-1)

$\varepsilon_3 = (^{15}\alpha_{NO3/NO2} - 1)$ (Eq. 3-2)

$\delta^{15}N\ (HNO_3)\ (R8) = \delta^{15}N\ (NO_3^-)\ (R8)$ (Eq. 3-3)

Therefore, the $\delta^{15}N\ (NO_x)$ in the atmosphere can be expressed using measured $\delta^{15}N\ (NO_3^-)$ and the net N isotope fractionation effect, ε_N.

$\delta^{15}N\ (NO_x)_{atmosphere} = \delta^{15}N\ (NO_3^-)_{measured} - \varepsilon_N$ (Eq. 4-1)

$\varepsilon_N = \varepsilon_1 \times f_1 + \varepsilon_2 \times f_2 + \varepsilon_3 \times f_3$ (Eq. 4-2)

, where ε_1, ε_2, and ε_3 are abovementioned N isotope fractionation effect of pathways (i), (ii), and (iii), respectively, and the proportional contributions (f_1, f_2, and f_3) of the three NO_3^- formation pathways

were estimated from $\Delta^{17}O$ measurements (Sect. 2.3.2).

2.3.2. Proportional contributions of three formation pathways to atmospheric particulate NO_3^-: $\Delta^{17}O$ (NO_3^-)

Due to its mass-independent nature, $\Delta^{17}O$ of particulate NO_3^- is a conservative tracer of photochemical NO_3^- formation (Michalski et al., 2003, 2004). At photochemical steady state, the $\Delta^{17}O$ of NO_2 is determined by the relative production rate of NO_2 via O_3 oxidation (R1) in NO_2 production (R1 and R2) (f_{O3}) and the mass-independent $\Delta^{17}O$ anomaly transferred from O_3 during R1 ($\Delta^{17}O\text{-}O_3^*$):

$$\Delta^{17}O\ (NO_2)\ (‰) = f_{O3} \times \Delta^{17}O\text{-}O_3^* \quad \text{(Eq. 5)}$$

f_{O3} was adopted from a previous study conducted in Beijing (Wang et al., 2019b), where the seasonal mean was 0.858 and 0.918 for summer and winter, respectively. $\Delta^{17}O\text{-}O_3^*$ can be approximated as 1.5 $\times$ $\Delta^{17}O\text{-}O_3$ because of the isotopic asymmetry of O_3 (Michalski and Bhattacharya, 2009). In this study, the $\Delta^{17}O\text{-}O_3^*$ is 37.5 ± 2.2‰ (mean ± SD) averaged from literature sources as the isotopic composition of ozone shows a remarkable stability in the lower troposphere (Ishino et al., 2017; Vicars et al., 2012; Vicars and Savarino, 2014)

The $\Delta^{17}O$ of particulate NO_3^- produced via the three formation pathways can be predicted by distinct $\Delta^{17}O$ transfer functions as the following (Morin et al., 2011):

$$\Delta^{17}O\ (NO_3^-)\ (1)\ (‰) = 2/3\ \Delta^{17}O(NO_2) = 2/3\ f_{O3} \times \Delta^{17}O\text{-}O_3^* \quad \text{(Eq. 6-1)}$$

$$\Delta^{17}O\ (NO_3^-)\ (2)\ (‰) = 5/6\ \Delta^{17}O(N_2O_5) = 1/3\ \Delta^{17}O(NO2) + 1/2\ \Delta^{17}O(NO_3) = 1/6\ \Delta^{17}O\text{-}O_3^*\ (4\ f_{O3} + 1) \quad \text{(Eq. 6-2)}$$

$$\Delta^{17}O\ (NO_3^-)\ (3)\ (‰) = \Delta^{17}O(NO_3) = 2/3\ \Delta^{17}O(NO_2) + 1/3\ \Delta^{17}O\text{-}O_3^* = 1/3\ \Delta^{17}O\text{-}O_3^*\ (2\ f_{O3} + 1) \quad \text{(Eq. 6-3)}$$

Finally, the $\Delta^{17}O$ (NO_3^-) can be expressed as the following:

$$\Delta^{17}O\ (NO_3^-)_{measured} = \Delta^{17}O\ (NO_3^-)\ (R4) \times f_1 + \Delta^{17}O\ (NO_3^-)\ (R7) \times f_2 + \Delta^{17}O\ (NO_3^-)\ (R8) \times f_3 \quad \text{(Eq. 7)}$$

where $\Delta^{17}O\ (NO_3^-)_{measured}$ is the measured value in this study and the three endmember values of $\Delta^{17}O\ (NO_3^-)$ (R4), $\Delta^{17}O\ (NO_3^-)$ (R7), and $\Delta^{17}O\ (NO_3^-)$ (R8) are calculated using Eqs. (6-1 to 6-3). The proportional contributions of the three NO_3^- formation pathways ($f_1 + f_2 + f_3 = 1$) were estimated by the SIAR model (Sect. 2.5.) for the winter and the summer months.

2.4. Estimation of $PM_{2.5}$ Aerosol Liquid Water Content (ALWC) and aerosol pH

ISORROPIA-II is a thermodynamic equilibrium model for the Cl^-, NO_3^-, SO_4^{2-}, Na^+, NH_4^+, K^+, Ca^{2+}, Mg^{2+}, and H_2O aerosol system (Fountoukis and Nenes, 2007). In the present study, the model was run as a "forward" and "metastable" mode to calculate aerosol liquid water content (ALWC) and pH. The detailed information of the model is found in Fountoukis and Nenes (2007). As input parameters, the concentrations of water-soluble ions that were measured by NIER and ambient RH and temperature were used for the model.

2.5. Bayesian stable isotope mixing model (stable isotope analysis in R, SIAR)

For quantifying proportional contribution of three NO_3^- formation pathways (f_1, f_2, and f_3 in Eq. 4-2), we used the Bayesian stable isotope mixing model (Parnell et al., 2013) implemented using the SIMMR package in R software, which is available at https://cran.r-project.org/web/packages/simmr/index.html. The Bayesian Markov Chain Monte Carlo approach is adequate to provide the relative contribution of the endmembers. Detailed information of the SIAR can be found in Parnell et al. (2010). As input data, measured $\Delta^{17}O\ (NO_3^-)$ and estimated $\Delta^{17}O\ (NO_3^-)$ endmember values of each pathway were treated in SIAR model. Similar use of the SIAR model can be found elsewhere (Song et al., 2020; Wang et al., 2019b).

2.6. Backward airmass trajectory

Two-day air mass backward trajectories were analyzed using the HYSPLIT (Hybrid Single-Particle Lagrangian Integrated Trajectory) model with meteorological input from the global data assimilation system (a regular 1° x 1° longitude-latitude grid) (Stein et al., 2015;

https://ready.arl.noaa.gov/HYSPLIT.php) . The trajectories were calculated every 6 h at an elevation of 500 m above sea level. The potential source contribution function (PSCF) was then applied to calculate the probable source location (latitude *i* and longitude *j*), which is determined here as the ratio of the number of trajectory end points associated with measured $\delta^{15}N$ (NO_3^-) values higher than a threshold value (set to 95th percentile of $\delta^{15}N$ (NO_3^-) (m_{ij}) to the total number of points (n_{ij}) in the *i j* th grid cell). The PSCF calculation was made in the openair package, R software (https://cran.r-project.org/web/packages/openair/index.html) (Carslaw and Ropkins, 2012).

3. Results and discussion

3.1. Seasonal characteristics of $PM_{2.5}$ concentration, $\delta^{15}N$ (NO_3^-), and $\Delta^{17}O$ (NO_3^-)

$PM_{2.5}$ mass concentration varied from 7.5 μg m^{-3} to 139.0 μg m^{-3} for the whole sampling period. According to the typical synoptic weather patterns of East Asia (Kim et al., 2007), the measurements are divided into summer (May-Aug) and winter (Oct.-Mar.) groups. A clear seasonal difference in $PM_{2.5}$ concentration and its composition were observed with significantly higher concentrations of mass and inorganic constituent in the winter than in the summer (Table 1 and Figure S1).

During the summer, $PM_{2.5}$ concentration ranged from 7.5 μg m^{-3} to 34.5 μg m^{-3} with a mean of 22.7 ± 6.9 μg m^{-3}. The mean concentration of TC and TN was 4.6 ± 1.4 μgC m^{-3} and 1.9 ± 1.0 μgN m^{-3}, respectively, resulting in the mean TC/TN ratio of 2.7 ± 2.0. The mass concentrations of all measured species were much higher in the winter, during which $PM_{2.5}$ concentration was raised up to 139.0 μg m^{-3} from 10.6 μg m^{-3} with a mean of 61.7 ± 39.2 μg m^{-3}. Accordingly, the mean of TC and TN was 15.2 ± 4.5 μgC m^{-3} and 11.8 ± 7.7 μgN m^{-3}, respectively and the mean TC/TN ratio of 0.9 ± 0.7 was noticeably lower than that of the summer.

For the entire experiment, the mean mass fraction against $PM_{2.5}$ was the highest for NO_3^- (26% ± 23%), followed by SO_4^{2-} (20% ± 1%) and NH_4^+ (14% ± 1%), highlighting the contribution of SIA to $PM_{2.5}$ mass. The NO_3^- mass concentration varied from 0.2 μg m^{-3} to 69.3 μg m^{-3} with a mean of 17.6 ± 22.1 μg m^{-3}. Seasonally, the NO_3^- concentration was significantly higher in the winter (29.7 ± 22.1 μg m^{-3}) than summer (0.8 ± 0.9 μg m^{-3}). TN existed completely as inorganic N from both NO_3^- and NH_4^+ during the winter (regression slope of 1.0). During the summer, NO_3^- and NH_4^+ comprised 67% of TN and the rest (33 %) was assumed to be organic nitrogen (ON) components. In contrast, the mass fraction of

SO_4^{2-} against $PM_{2.5}$ was higher in the summer (23%) than winter (19%). The seasonal characteristics of chemical composition implies the significant role of inorganic nitrogen species in $PM_{2.5}$ mass increase in winter and ON and sulfate in summer.

Both $\delta^{15}N$ (NO_3^-) and $\Delta^{17}O$ (NO_3^-) exhibited an inverse correlation with ambient temperature (r= -0.87 and r= -0.55, respectively). The $\delta^{15}N$ (NO_3^-) exhibited higher values in winter with a weight-mean of -0.7‰ ± 3.3 ‰ and 3.8‰ ± 3.7 ‰ in the summer and the winter, respectively. This seasonal pattern of $\delta^{15}N$ (NO_3^-) has been typically observed in East Asia regions (Li et al., 2019; Song et al., 2019; Zong et al., 2020). Analysis of backward airmass trajectory indicates that the lower and the upper bound of $\delta^{15}N$ (NO_3^-) were associated with air masses from the ocean by southerly and easterly winds in the summer and from Siberia by northerly winds in winter, respectively (Figure S3). In comparison with urban China (Figure 2a), averaged summer $\delta^{15}N$ (NO_3^-) values were comparable between Seoul and all urban Chinese sites reported here, whereas in winter, $\delta^{15}N$ (NO_3^-) of Seoul was similar to those of Shanghai and Guangzhou rather than $\delta^{15}N$ (NO_3^-) of Beijing that were higher than 10‰. Another observation at a mountain station in Taiwan shows that the highest $\delta^{15}N$ (NO_3^-) was found in spring when the level of anthropogenic constituents were elevated (Guha et al., 2017). These observations over East Asia may suggest at some extent that the seasonal pattern of $\delta^{15}N$ (NO_3^-) is basically associated with synoptic meteorological condition that controls the type and strength of emission sources, where low and high $\delta^{15}N$ (NO_3^-) values indicate biogenic soil emissions and fossil-combustion, respectively. (Elliott et al., 2019)

Along with nitrogen isotope, heavier oxygen isotopes were also enriched in NO_3^- during the winter compared to the summer, when the weight-mean of $\delta^{17}O$, $\delta^{18}O$, and $\Delta^{17}O$ in NO_3^- were 70.4‰ ± 5.4 ‰, 82.0‰ ± 6.2 ‰, and 27.7‰ ± 2.2 ‰ for the winter and 57.3‰ ± 4.9 ‰, 65.7‰ ± 6.2 ‰, and 23.2‰ ± 2.2 ‰ for the summer. These results of high winter and low summer $\Delta^{17}O$ (NO_3^-) were consistent with previous observations at urban Beijing (He et al., 2018; Wang et al., 2019b; Figure 2b), indicative of relatively greater contribution of nighttime oxidation pathways in winter. It is also noteworthy that our summer and winter $\Delta^{17}O$ (NO_3^-) values were similar to annual $\Delta^{17}O$ (NO_3^-) values of an urban (Sapporo) and a rural (Rishiri) site in Japan, respectively (Nelson et al., 2018). It is likely suggestive that the winter $\Delta^{17}O$ value in Seoul has undergone a considerable atmospheric processing on a regional scale.

Given that $PM_{2.5}$ concentrations reflect the seasonality, atmospheric chemical composition and meteorological properties were examined in relation to $PM_{2.5}$ concentrations (Figure 3). Clearly, for the winter samples with $PM_{2.5}$ concentration greater than 40 μg m^{-3}, meteorological conditions varied

relative to low $PM_{2.5}$ samples; relatively high temperature and RH staying at 0 °C to 10 °C and 45 % to 65 %, respectively, and low wind speed of 1 m s^{-1} to 2 m s^{-1}, representing the meteorological characteristics of winter $PM_{2.5}$ episodes. Particularly in winter, a strong linearity of $PM_{2.5}$ was found with most chemical constituents considered in this study, such as SIA species, TN, NOR, and SOR. However, although being elevated in levels, NO_2 and O_3 mixing ratios showed non-linearity with $PM_{2.5}$ concentrations. Isotope ratios were correlated either linearly or inversely with $PM_{2.5}$ concentrations. In winter, $\Delta^{17}O$ (NO_3^-) showed the best correlation with $PM_{2.5}$ concentrations but $\delta^{15}N$ (NO_3^-) was inversely related with $PM_{2.5}$ level.

3.2. Graphical representation of dual isotopes: $\Delta^{17}O$ and $\delta^{15}N$ of NO_3^-

The isotope ratios of source endmembers are scarce in the study region and in the aerosol measurements and the isotope fractionation effect during gas-to-particle conversion is often estimated with thermodynamic constants and reasonable assumptions. In this regard, the graphical representation of dual isotopes enables the complex signatures of atmospheric samples to be distinguished and allows their oxidation processes to be constrained. Figure 4 displayed measured $\delta^{15}N$ (NO_3^-) and $\Delta^{17}O$ (NO_3^-) coordinates with related chemical parameters in colors.

In Figure 4a and b, the range of $\Delta^{17}O$ (NO_3^-) endmembers for the three NO_3^- oxidation pathways calculated in Sect. 2.3.2. were presented by black dotted boxes, of which domains of the three pathways are successfully distinguished. The $\Delta^{17}O$ (NO_3^-) of all samples fell into the predicted ranges of the $\Delta^{17}O$ endmembers, but were separated into seasonal groups. Most of summer $\Delta^{17}O$ (NO_3^-) values indicate NO_3^- (R4) pathway. It is in accordance with what has been reported in temperate areas during summer (Alexander et al., 2009; Michalski et al., 2003). In field measurements of $\delta^{15}N$ (NO_3^-) and $\delta^{18}O$ (NO_3^-) in Chinese cities, the proportional contribution of OH-oxidation pathway was significantly correlated with latitudes (Zong et al., 2020), confirming the evidence of the NO_3^- formation through OH oxidation depending on UV radiation intensity.

In comparison, more than half of winter samples are located in the domain indicating NO_3^- (R7) and (R8) pathways. Particularly, for winter samples with NO_3^- mass concentration higher than ~ 30 μg m^{-3}, $\Delta^{17}O$ (NO_3^-) values clearly represent the (R7) pathway. The winter $\Delta^{17}O$ (NO_3^-) was proportional to nitrogen oxidation ratio (NOR, Figure 4c), indicative of efficient conversion of NO_x to NO_3^- via O_3 oxidation pathways. In the summer periods when NO_3^- concentrations were relatively high (above ~ 3 μg m^{-3}), the contributions of O_3 oxidation pathways became elevated, which is a similar pattern to what

was observed in the winter. This result suggests that the O_3 oxidation pathways are likely to be responsible for the rapid conversion of particulate NO_3^- observed during winter and summer $PM_{2.5}$ episodes in the study region.

The formation of N_2O_5 (R6) is dependent on both NO_2 and O_3, which are reciprocally correlated in source regions. The equilibrium of R6 shifts to N_2O_5 at low temperature and its lifetime against photolysis is long under the low sunlight. For these reasons, the dark formation of NO_3^- (R7) would be favorable in urban outflows in winter. The hydrolysis of N_2O_5 on aerosol surface (R7) is highly dependent on RH, aerosol liquid water content (AWLC), and chemical composition (Hallquist et al., 2003; Wahner et al., 1998). To evaluate the $\Delta^{17}O$ (NO_3^-) signature observed, we calculated ALWC and acidity of aerosol, pH using ISORROPIA II model (Sect. 2.4.). Given the high concentration of nano-particles from various sources in the urban areas, it is assured that aerosol surface is enough for NO_3^- (R7) pathway. The calculated ALWC was higher by 90 % (19.1 ± 22.8 μg m^{-3}) in the winter and lower by 21 % (7.8 ± 5.2 μg m^{-3}) in the summer relative to the annual mean of the two years. When NO_3^- mass concentrations were greater than ~ 3 μg m^{-3} in the summer and ~ 30 μg m^{-3} in the winter, ALWC was 14.3 μg m^{-3} and 31.7 μg m^{-3}, respectively, which were greater by 166 % and 183 % than the seasonal mean, respectively (Figure 4d). Furthermore, the high $\Delta^{17}O$ (NO_3^-) and ALWC coincided with lower bound (about 4) of winter pH varying from 4 to 6, whereas aerosol pH was 2-3 during the summer. The low aerosol pH concurrent with the high $\Delta^{17}O$ (NO_3^-) and ALWC is coherent with the aqueous-phase HNO_3 formation on liquid aerosol through R7.

While $\Delta^{17}O$ (NO_3^-) allows insights into the oxidation pathway of NO_3^-, $\delta^{15}N$ (NO_3^-) values are affected by various factors, most of which are not well constrained due to the complicated chemistry and key roles of nitrogen oxides in the Earth's environment. In this study, $\delta^{15}N$ (NO_3^-) variability versus $PM_{2.5}$ concentration resembled the variability of NO_2 versus $PM_{2.5}$ concentration (Figure 3f and o), implying a close link between NO_2 oxidation and $\delta^{15}N$ (NO_3^-). Therefore, in addition to the role of $\Delta^{17}O$ (NO_3^-) as a tracer of NO_3^- oxidation pathway, we evaluated whether a variation of $\delta^{15}N$ (NO_3^-) indicates NO_x oxidation efficiency between NO and NO_2 (Freyer et al., 1993; Nelson et al., 2018; Walters et al., 2016). A possible effect on $\delta^{15}N$ during NO_x photochemical cycling cannot be predicted in the same way under varying conditions, e.g., depending on abundances of NO, NO_2, and O_3. The shift in $\delta^{15}N$ (NO_2) relative to $\delta^{15}N$ (NO_x) in the atmosphere will change depending on f_{NO2} and temperature-dependent $\alpha_{NO2/NO}$ (Freyer et al., 1993; Li et al., 2020; Walters et al., 2016). When O_3 mixing ratio is high, NO is almost completely oxidized to NO_2, leading to an increasing f_{NO2} value, and the $\delta^{15}N$ (NO_2) should correspond to the $\delta^{15}N$ of NO_x sources (Freyer et al., 1993).

In the dual isotope coordinates of $\delta^{15}N$ (NO_3^-) and $\Delta^{17}O$ (NO_3^-) (Figure 4), it is evident the samples taken during a record-breaking winter $PM_{2.5}$ pollution events are associated with the lower bound values of $\delta^{15}N$ (NO_3^-) (-1 to 4 ‰) and the highest $\Delta^{17}O$ (NO_3^-) values (28 to 31 ‰). Simultaneous measurements of PM_1 chemical composition in Seoul and Beijing demonstrated that the regionally-processed air masses were long-range transported to Seoul within approximately 2 days during these episodes (Kim et al., 2020a). Their NO_2/O_3 ratio (1 to 2) was clearly lower with higher f_{NO2} (0.7 to 0.8) compared to the other winter samples (Figure 4g and h). This result implies that O_3 level was high enough to efficiently oxidize NO to NO_2 during the severe $PM_{2.5}$ pollution events. In this condition, the shift in $\delta^{15}N$ (NO_2) relative to $\delta^{15}N$ (NO_x) is insignificant and consequently, $\delta^{15}N$ (NO_2) would be lower than those of other winter samples unless both emission sources and $\alpha_{NO2/NO}$ changed significantly. Considering that NO_3^- is the key driver of the high $PM_{2.5}$ in Seoul, the higher degree of NO_x oxidation efficiency is worth highlighting, in conjunction with a strong linear relationship between $\Delta^{17}O$ (NO_3^-) and NOR (Figure 4c) revealing an efficient conversion of NO_2 to NO_3^- through NO_3^- pathway (R5+R6+R7+R8) via O_3. The seasonally bifurcated $\delta^{15}N$ (NO_3^-) can be attributed primarily to the NO_x sources, which will be discussed in Section 3.4.

3.3. Contributions of major HNO_3 oxidation pathways

Combining the $\Delta^{17}O$ (NO_3^-) measurements and the calculation of $\Delta^{17}O$ transferred from O_3 to HNO_3, the contributions of three major NO_3^- formation pathways were quantitatively accounted, despite the inherent uncertainties in the calculation (Sect. 2.5.).

NO_3^- pathway (R4) dominated the total NO_3^- formation (87 ± 6 %) in summer. In contrast, the nighttime pathways through N_2O_5 and NO_3 (pathways R7 and R8) were responsible for 24 % and 14 % of the NO_3^- formation in the winter, respectively. The contribution increased further to 40 % and 30 %, respectively, on haze days when $PM_{2.5}$ concentration exceeded 75 μg m^{-3}, national air quality standard for "very bad" alert. The significant nighttime oxidation of NO_3^- has been observed broadly at urban sites in Northeast Asia. The results of this study are consistent with those conducted in Beijing, showing low $\Delta^{17}O$ values in summertime (about 17 ‰ to 25 ‰) and substantially high $\Delta^{17}O$ values (about 25 ‰ to 34 ‰) in wintertime when NO_3^--driven $PM_{2.5}$ haze pollution occurred (He et al., 2018; Song et al., 2020; Wang et al., 2019b). In general, nighttime pathways accounted for more than 60 % and up to 97 % in Beijing (He et al., 2018; Song et al., 2020; Wang et al., 2019b). From a global perspective, the chemical transport model demonstrated that N_2O_5 heterogeneous hydrolysis was comparably important

as NO_2 + OH (41 %) for NO_3^- formation at below 1km altitude (Alexander et al., 2020).

It is noteworthy that although the seasonal patterns are similar in Northeast Asia, the average proportional contributions estimated from $\Delta^{17}O$ (NO_3^-) are highly sensitive to input parameters (i.e., f_{O3} and $\Delta^{17}O$-O_3*). In this study, the seasonal f_{O3} was assumed to be equal to those estimated for Beijing and set to 0.858 ± 0.05 and 0.918 ± 0.05 for the warm and cold months, respectively (Wang et al., 2019b), which are comparable to other estimates for Beijing (0.86) and Shanghai (0.97) (He et al., 2018, 2020) and the annual-mean of 0.85 in a global model (Alexander et al., 2020).

The uncertainty associated with $\Delta^{17}O$-O_3* has been recognized as the largest source of uncertainty in estimating NO_3^- production pathways from $\Delta^{17}O$ (NO_3^-) (Alexander et al., 2009, 2020). In this study, the $\Delta^{17}O$-O_3* of 37.5 ± 2.2 ‰ was averaged from previous observations, corresponding to $\Delta^{17}O$-bulk O_3 of 25 ‰ (Ishino et al., 2017; Vicars et al., 2012; Vicars and Savarino, 2014). Our mean $\Delta^{17}O$-O_3* of 37.5 ‰ was 2.8 ‰ higher and 1.5 ‰ lower than what was used in the field studies (Song et al., 2020; Wang et al., 2019b) and the studies (He et al., 2018, 2020), respectively, for urban Beijing and Shanghai. When sensitivity test was conducted for the proportional contribution of the three oxidation pathways, a 2.8 ‰ change in $\Delta^{17}O$-O_3* value caused 1.6 ‰, 2.1 ‰, and 2.5 ‰ change in the endmember for (R4), (R7), and (R8) pathway, respectively. As a result, the average contribution of the nighttime pathways, including NO_3^- (R7) and NO_3^- (R8), increased to 23 % in summer and 65 % in winter. This suggests that a proper use of key parameters driving endmember values is pre-requisite for more realistic quantification of NO_3^- oxidation pathway contributions.

3.4. Major NO_x emission sources

To investigate major emission sources of atmospheric NO_x in Seoul, $\delta^{15}N$ (NO_x) in the atmosphere ($\delta^{15}N$ $(NO_x)_{atmosphere}$) was estimated from measured $\delta^{15}N$ (NO_3^-) considering nitrogen isotopic fractionation effects (ε_N) based on a dual isotopes approach ($\Delta^{17}O$ and $\delta^{15}N$). Estimated ε_N values were 5.9 ± 1.5 ‰ and of 12.2 ± 0.5 ‰ and accordingly, the $\delta^{15}N$ $(NO_x)_{atmosphere}$ was -8.7 ± 3.3 ‰ and -5.8 ± 4.2 ‰ in summer and winter, respectively. The larger winter ε_N reveals the enhanced contribution of nighttime oxidation pathway via N_2O_5. As a result, a seasonal difference in $\delta^{15}N$ $(NO_x)_{atmosphere}$ was as small as 2.9 ‰ on average, which is suggestive of little seasonal difference in major NO_x emission source in Seoul.

Figure 5 displays the measured $\delta^{15}N$ (NO_3^-) and estimated $\delta^{15}N$ $(NO_x)_{atmosphere}$ of individual samples

together with $\delta^{15}N$ (NO_x) domains of emission source endmembers reported in literature; biogenic soil (driven by fertilizer use; -35.1 ± 10.2 ‰) (Felix and Elliott, 2014; Li and Wang, 2008; Yu and Elliott, 2017), biomass burning (1.8 ± 1.8 ‰) (Fibiger and Hastings, 2016), vehicle emissions (-2.5 ± 1.5 ‰) (Walters et al., 2015), and coal combustion (14.2 ± 4.5 ‰) (Felix et al., 2012; Heaton, 1990). Both in summer and winter, $\delta^{15}N$ $(NO_x)_{atmosphere}$ are the closest to the domain of vehicle emissions $\delta^{15}N$ (NO_x), highlighting the largest contribution of vehicle emissions to NO_x in Seoul (Figure 5). However, the winter $\delta^{15}N$ (NO_3^-) without isotope fractionation effect apparently point to coal emissions, which could lead to misleading conclusions about major NO_x sources. This result is supported by a better correlation of NO_2 with CO than with SO_2 for both seasons. According to a (anthropogenic) bottom-up emissions inventory, the Clean Air Policy Support System (CAPSS), total mobile sources account for about two-third of NO_x emissions in Korea, followed by combustion sources such as energy and manufacturing industries (33 %). The highest NO_2 column densities are distinct in Seoul Metropolitan Areas (SMA), which is mostly due to the emissions from transportation (Kim et al., 2020b). Our results of the isotope measurements are in fairly good agreement with the national emission inventories and satellite observations, highlighting the largest contribution of vehicle emissions to NO_x sources in Seoul.

Other than vehicle emissions, the lower bound summer $\delta^{15}N$ $(NO_x)_{atmosphere}$ and the upper bound winter $\delta^{15}N$ $(NO_x)_{atmosphere}$ were relatively closer to the $\delta^{15}N$ (NO_x) of fertilized soil emissions and coal-combustion, respectively. These seasonally distinct contributions from soil emissions and coal combustion were consistent with the results from previous studies conducted in China, revealing common seasonal emission characteristics on a regional scale in East Asia. It was evident that the upper bound winter $\delta^{15}N$ $(NO_2)_{atmosphere}$ coincided with elevated SO_4^{2-}/ NO_3^- mass ratio by 2-3 times. During these periods, trajectory analysis indicates that air masses originated from cold regions in northeastern China, such as Liaoning province, where heavy and coal-fired industries are located. In Beijing located in northeastern China, coal combustion is an important fossil-fuel source as the highest contribution source to atmospheric NO_x emissions during winter, about 30 to 40 %, regardless of approaches used for estimating NO_3^- oxidation pathways, either $\Delta^{17}O$ or $\delta^{18}O$ (Li et al., 2019; Song et al., 2019, 2020; Zong et al., 2020). Thus, in this study, the upper bound winter $\delta^{15}N$ $(NO_x)_{atmosphere}$ suggests enhanced contributions of coal combustion to atmospheric NO_x emissions. It is particularly noteworthy that the lower winter $\delta^{15}N$ (NO_3^-) and thus relatively lower contribution of coal combustion confirms the recent trend that emissions from coal combustion have been reduced in China (Cheng et al., 2019; Tong et al., 2018). Our study was conducted in later years (2018-2019) than their studies (2013-2017), of which $\delta^{15}N$ (NO_3^-) values were rather comparable to the winter mean $\delta^{15}N$ (NO_3^-) observed in Seoul during January 2014 ~ February 2016 (11.9 ± 2.5 ‰; Park et al., 2018). The lower bound of winter $\delta^{15}N$ (NO_3^-)

values associated with the highest NO_3^- and $PM_{2.5}$ concentrations (Figures 3 and 4) was considered a result of complex effects of isotopic fractionation, as discussed above.

This study region is under influence of various biomass burning sources throughout a year, such as agricultural combustion in vicinities of Seoul and over eastern China from spring to fall (Chen et al., 2017; Zhao et al., 2017), wild fires over Siberia and Russian Far East in summer (van der Werf et al., 2010), and residential biomass combustion for heating over east Asia in winter. Some winter $\delta^{15}N$ $(NO_x)_{atmosphere}$ values fell in the $\delta^{15}N$ (NO_x) range of biomass burning endmember (Fibiger and Hastings, 2016; Figure 5). When assessing contributions of biomass burning based on $\delta^{15}N$ $(NO_x)_{atmosphere}$ and few endmember $\delta^{15}N$ (NO_x), however, caution should be exerted considering the fact that $\delta^{15}N$ (NO_x) varied among biomass types from -7 to 12‰ (Fibiger and Hastings, 2016) and there is currently a lack of understanding of biomass combustion that could potentially affect air quality in Seoul.

5134. Conclusions and outlook

5145. Our $\delta^{15}N$ and $\Delta^{17}O$-based study confirms that vehicle emissions are the main source of NO_3^- in $PM_{2.5}$ in Seoul during the summer and the winter. In addition, the qualitative estimates of NO_x emission sources provide suggestive evidence for enhanced contributions from coal combustion and biogenic soil emissions in the winter and the summer, respectively. Moreover, severe winter haze events with daily $PM_{2.5}$ exceeding 100 μg m^{-3} were mainly driven by NO_3^- (up to ~60 % in $PM_{2.5}$). Reducing NO_x emissions from vehicles is, therefore, essential for an effective mitigation measure to improve fine aerosol pollution in the study region. Particularly, the highest $PM_{2.5}$ was concurrent with the highest NOR and $\Delta^{17}O$ (NO_3^-), and the lowest $\delta^{15}N$ (NO_3^-), revealing the heterogeneous conversion of HNO_3 to particulate NO_3^- through O_3 oxidation pathway during the winter haze episodes. The multiple-isotope signatures of particulate NO_3^-, including ^{17}O, ^{18}O, and ^{15}N, highlight the secondary nature of fine aerosol pollution intimately coupled with the photochemical oxidation process.

While our results demonstrate that $\delta^{15}N$ and $\Delta^{17}O$ are robust tracers for major NO_x sources, quantitative source apportionment using the isotope method requires further elaboration of isotope equilibrium/kinetic fractionation effects involved in photochemical cycling of nitrogen oxides and $\delta^{15}N$ of NO_x source endmembers representing local or regional emissions in East Asia. In well-designed field studies, the $\delta^{15}N$ and $\Delta^{17}O$ measurements of multiphase and their vertical structures allow us to test the isotope fractionation effects suggested by laboratory experiments and theoretical calculations, and to

characterize the atmospheric processing that influence them. In addition, there is an urgent need to document the $\delta^{15}N$ (NO_x) values of emissions from vehicles with/without selective catalytic reduction (SCR) and from biomass combustion as a function of biomass type and combustion conditions. Consequently, a comprehensive and quantitative understanding of the oxidation pathways and emission sources of nitrogen oxides using $\delta^{15}N$ and $\Delta^{17}O$ measurements will be able to elucidate detailed mechanisms driving severe haze development in megacities of northeast Asia, including Seoul.

Acknowledgement

This research was supported by the National Strategic Project-Fine Particle of the National Research Foundation of Korea (NRF), funded by the Ministry of Science and ICT (MSIT), Ministry of Environment (ME), and Ministry of Health and Welfare (MOHW) (2017M3D8A1092015). Funding to S. Lim was provided by the National Research Foundation of Korea (NRF) from the Ministry of Science and ICT (2018R1D1A1B07050849). M. Lee thanks for the support from NRF (2020R1A2C3014592). J. Savarino thanks the French National Research Agency (Investissements d'avenir grant ANR-15-IDEX-02) and the INSU programme LEFE-CHAT for supporting the stable isotope laboratory. This is publication 4 of PANDA platform on which isotope analyses were performed.

548 **Table and figures**

549 **Tables**

550

551 **Table 1. Measurement summary of $PM_{2.5}$ chemical constituents and isotopic composition in Seoul**
552 **during the sampling period of May. 2018-Mar. 2019. Arithmetic mean ± 1 standard**
553 **deviation (mass fraction, %) for mass concentrations and concentration-weight mean ± 1**
554 **standard deviation for isotope ratios.**

555

Constituents	Summer (n = 13)	Winter (n = 18)
$PM_{2.5}$ (μg m^{-3})	22.7 ± 6.9	61.7 ± 39.2
TC	4. 6 ± 1.4 (20 %)	15.2 ± 4.5 (25 %)
TN	1.9 ± 1.0 (8 %)	11.8 ± 7.7 (19 %)
NO_3^-	0.8 ± 0.9 (4 %)	29.7 ± 22.1 (48 %)
NH_4^+	1.9 ± 0.8 (8 %)	11.7 ± 8.4 (19 %)
SO_4^{2-}	5.3 ± 2.1 (23 %)	11.5 ± 9.2 (19 %)
$[NH_4^+]/([SO_4^{2-}]+[NO_3^-])$ equiv. ratio	0.83 ± 0.08	0.94 ± 0.09
$\delta^{15}N$ (NO_3^-)	-0.7 ± 3.3	3.8 ± 3.7
$\delta^{17}O$	57.3 ± 4.9	70.4 ± 5.4
$\delta^{18}O$	65.7 ± 6.2	82.0 ± 6.2
$\Delta^{17}O$	23.2 ± 2.2	27.7 ± 2.2

556

557

Figures.

Figure 1. Location of the study region. (a) Seoul metropolitan area in South Korea and (b) sampling site of Korea University campus in the northeast Seoul.

Figure 2. (a) $\delta^{15}N$ (NO_3^-) and (b) $\Delta^{17}O$ (NO_3^-) $PM_{2.5}$ observed in Northeast Asia are compared: Seoul in this study (red), Beijing (brown), Shanghai (orange), and Guangzhou (light) in China, and Rishiri (green) and Sapporo (blue) in Japan during summer (circle) and winter (square). Marker indicates mean value (concentration-weighted average for Seoul samples in this study), and lower and upper whiskers denote minimum and maximum values (This study; He et al., 2018; Lim et al., 2020; Nelson et al., 2018), mean ± standard deviation (Song et al., 2019; Wang et al., 2019b), or 25th and 75th percentiles (Zong et al., 2020).

Figure 3. Relationships of $PM_{2.5}$ mass concentration with meteorological parameters (a-c), concentrations of reactive gases (d-f, k) and aerosol chemical constituents (g-j, l-n), and N and O isotopic compositions (o-q) measured in Seoul during the summer (open circle) and the winter (blue ribbon).

Figure 4. The relationship of measured $\delta^{15}N$ (NO_3^-) and $\Delta^{17}O$ (NO_3^-) values with key parameters during the summer (open circle) and winter (closed ribbon). The predicted $\Delta^{17}O$ (NO_3^-) values are presented as dotted rectangles for the tree major NO_3^- formation pathways (R4, R7, and R8, see Sect. 2.3.2 for details) in (a) summer and (b) winter. Data are color coded by (a) and (b) nitrate concentrations, (c) NOR, (d) ALWC, (e) pH, (f) $[NH_4^+]/([SO_4^{2-}]+[NO_3^-])$ equivalent ratio, (g) NO_2/O_3 ratio, and (h) f_{NO2}. Marker size is proportional to $PM_{2.5}$ concentration ranging from 10 μg m^{-3} to 100 μg m^{-3}.

Figure 5. Variations in measured $\delta^{15}N$ (NO_3^-) (open) and estimated $\delta^{15}N$ $(NO_x)_{atmosphere}$ (closed) in Seoul during the summer (circle) and winter (triangle). The $\delta^{15}N$ (NO_x) range (mean ± 1sd) of source end members are distinguished by dotted boxes in different colors: coal combustion (14.2 ± 4.5 ‰) (Felix et al., 2012; Heaton, 1990), biomass burning (1.8 ±1.8 ‰) (Fibiger and Hastings, 2016), vehicle emissions (-2.5 ± 1.5 ‰) (Walters et al., 2015), and biogenic soil emissions (-35.1 ± 10.2 ‰) (Felix and Elliott, 2014; Li and Wang, 2008; Yu and Elliott, 2017).

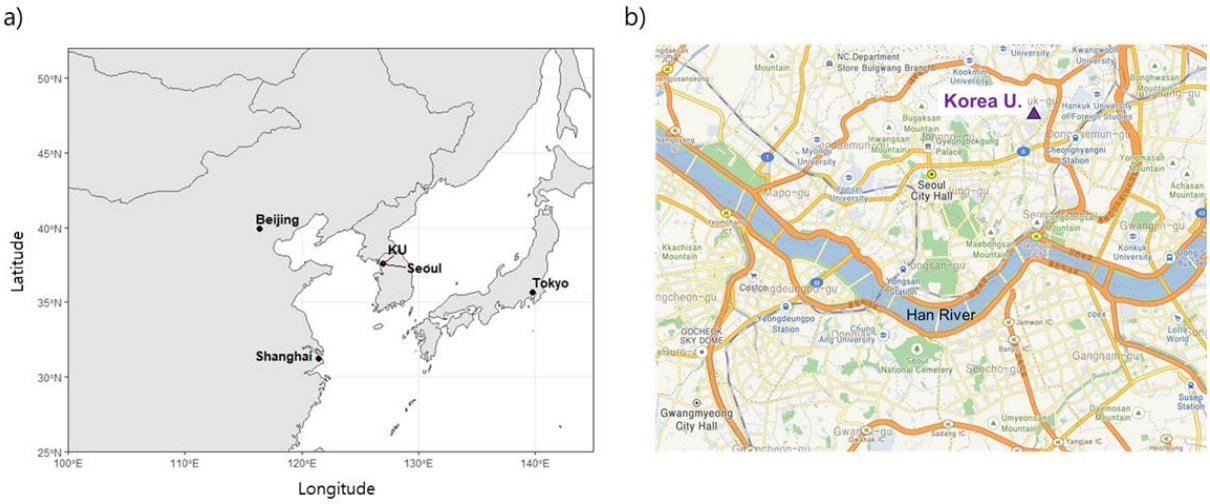

587

588 **Figure 1. Location of the study region. (a) Seoul metropolitan area in South Korea and (b)**
589 **sampling site of Korea University campus in the northeast Seoul.**

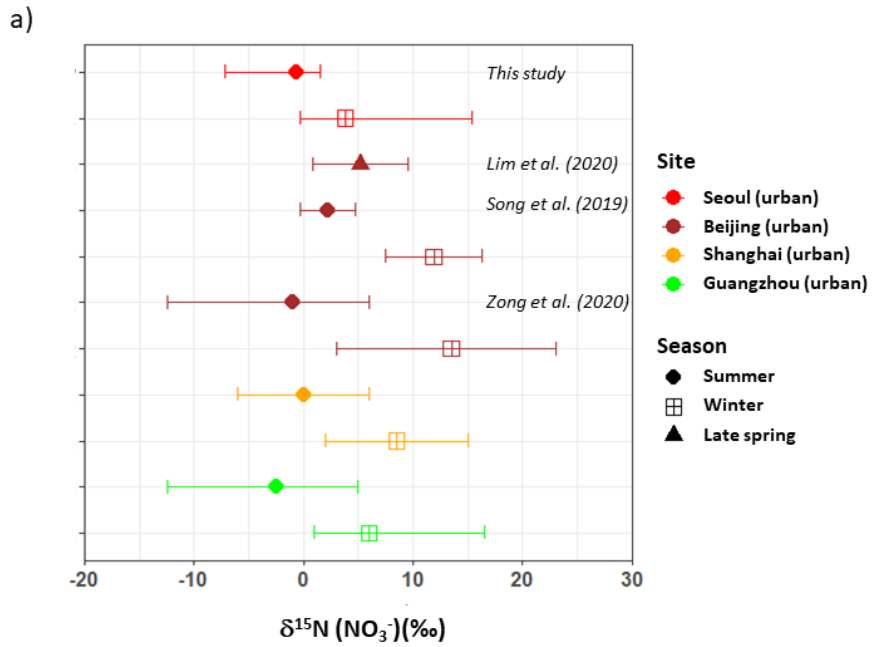

590

b)

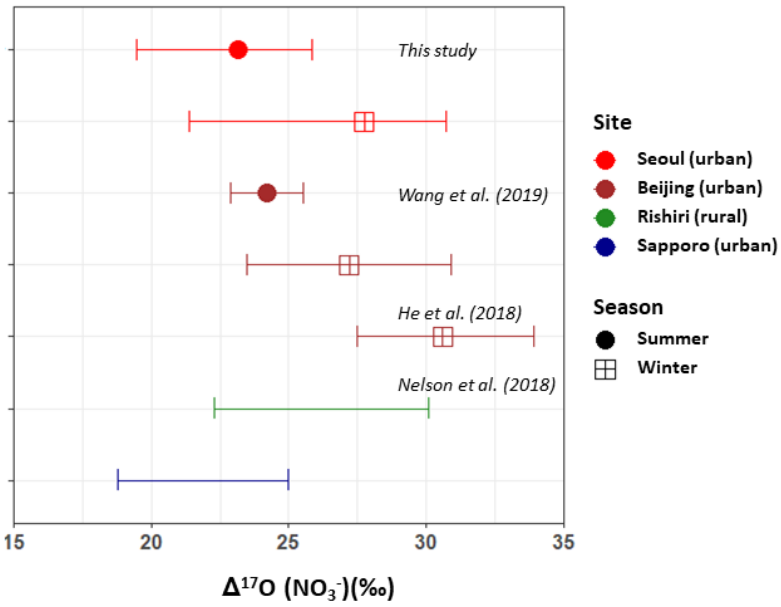

591

592 **Figure 2. (a) $\delta^{15}N$ (NO_3^-) and (b) $\Delta^{17}O$ (NO_3^-) $PM_{2.5}$ observed in Northeast Asia are compared:**
593 **Seoul in this study (red), Beijing (brown), Shanghai (orange), and Guangzhou (light) in**
594 **China, and Rishiri (green) and Sapporo (blue) in Japan during summer (circle) and**
595 **winter (square). Marker indicates mean value (concentration-weighted average for**
596 **Seoul samples in this study), and lower and upper whiskers denote minimum and**
597 **maximum values (This study; He et al., 2018; Lim et al., 2020; Nelson et al., 2018), mean**
598 **± standard deviation (Song et al., 2019; Wang et al., 2019b), or 25th and 75th percentiles**
599 **(Zong et al., 2020).**

600

601

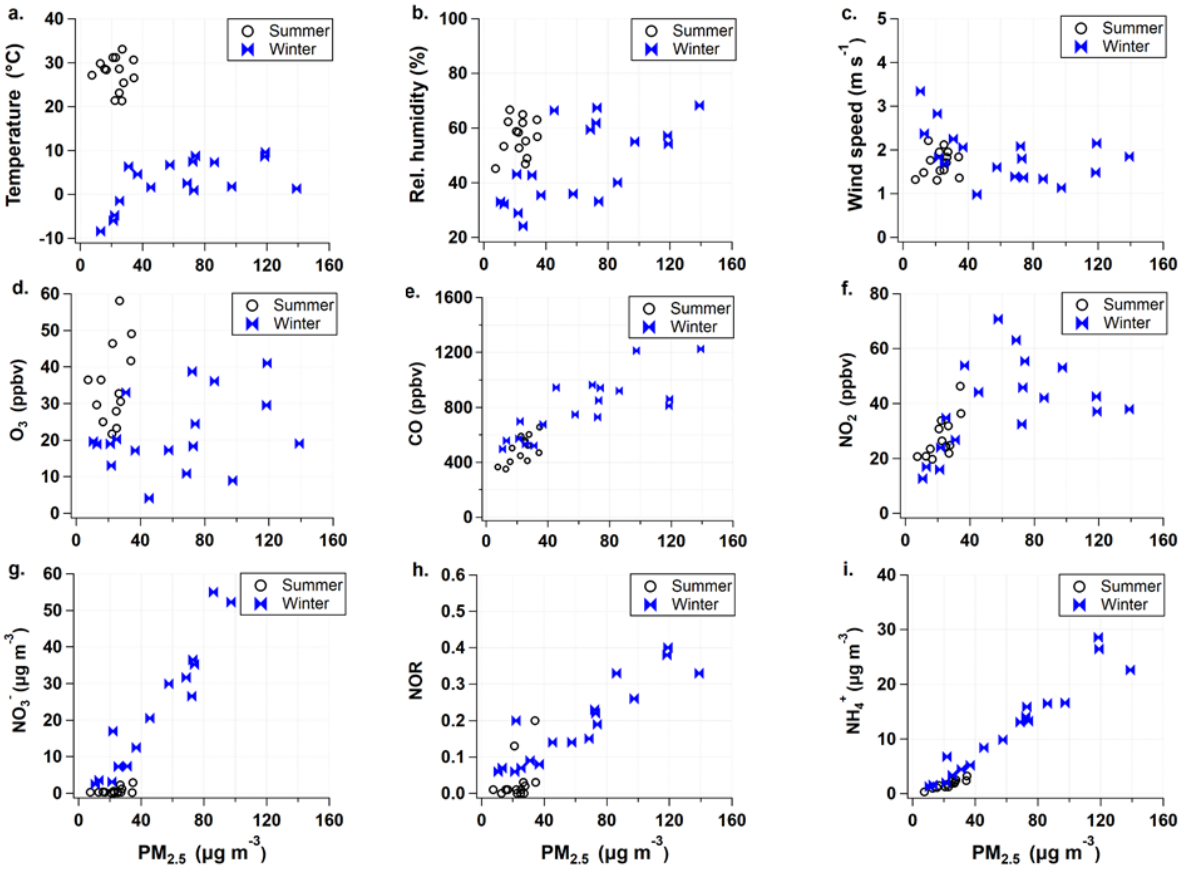
a.
Temperature (°C)
b.
Rel. humidity (%)
c.
Wind speed (m s-1)
d.
O3 (ppbv)
e.
CO (ppbv)
f.
NO2 (ppbv)
g.
NO3- (μg m-3)
h.
NOR
i.
NH4+ (μg m-3)
Summer
Winter
PM2.5 (μg m-3)

602

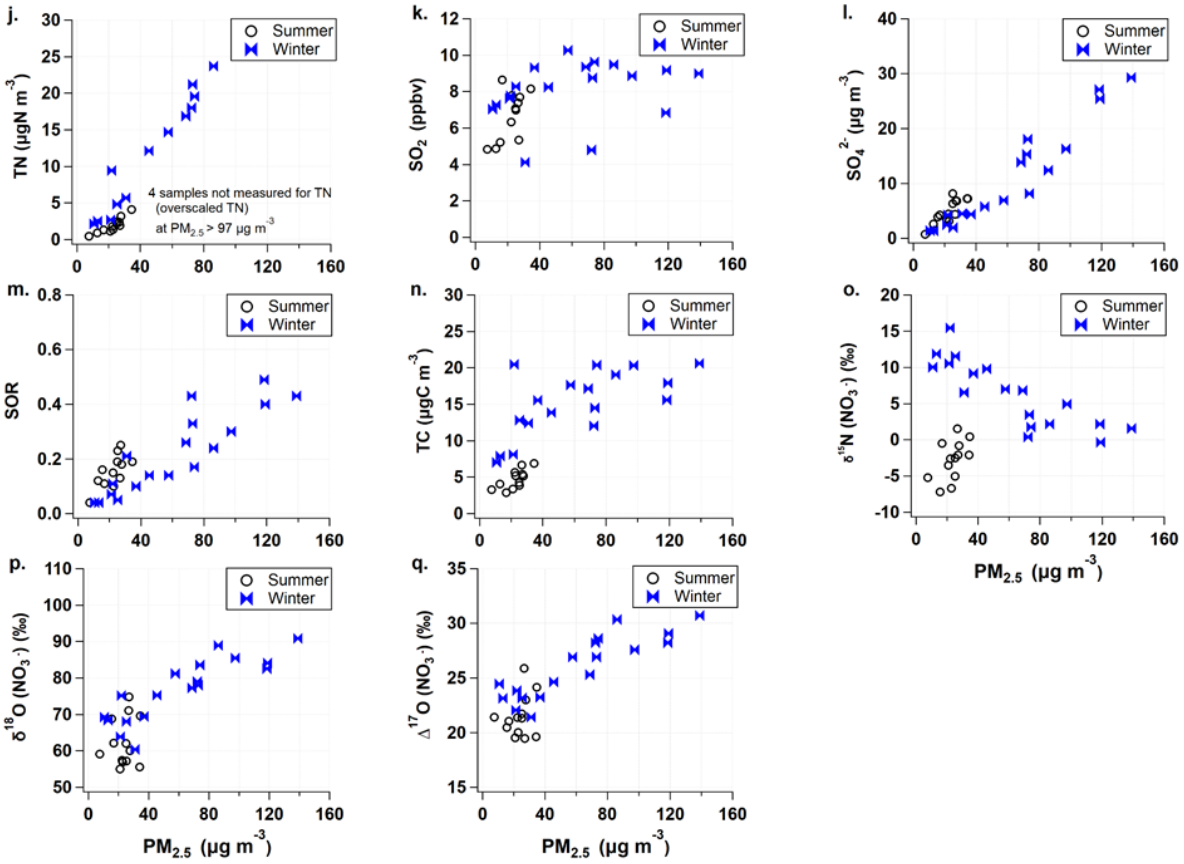

603

604 **Figure 3. Relationships of $PM_{2.5}$ mass concentration with meteorological parameters (a-c),**
605 **concentrations of reactive gases (d-f, k) and aerosol chemical constituents (g-j, l-n),**
606 **and N and O isotopic compositions (o-q) measured in Seoul during the summer (open**
607 **circle) and the winter (blue ribbon).**

608

609

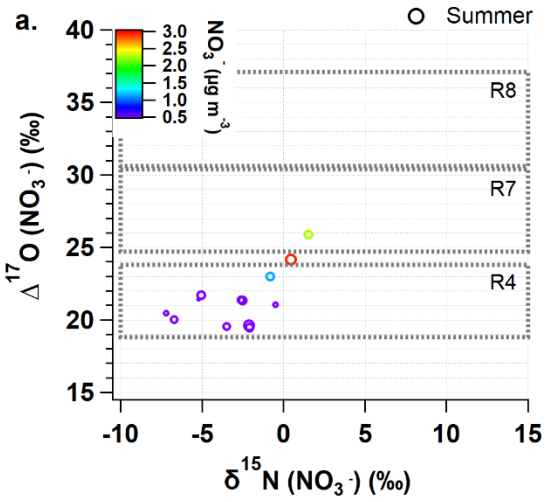
a.
Summer
R8
R7
R4
NO3- (μg m-3)
3.0
2.5
2.0
1.5
1.0
0.5
Δ17O (NO3-) (‰)
δ15N (NO3-) (‰)

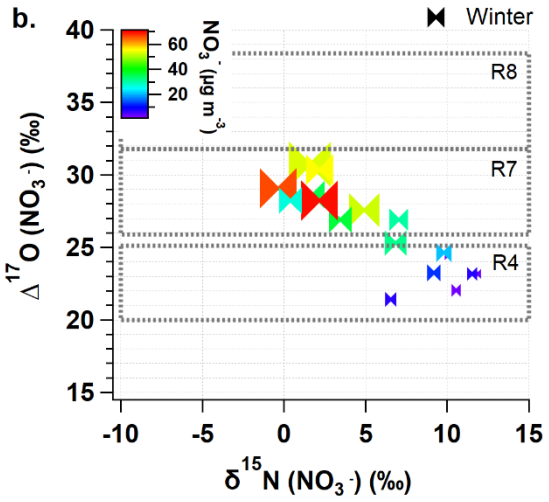
b.
Winter
R8
R7
R4
NO3- (μg m-3)
60
40
20
Δ17O (NO3-) (‰)
δ15N (NO3-) (‰)

610

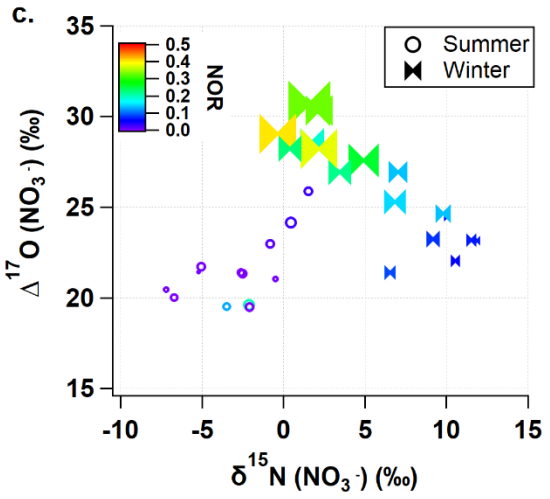
c.
Summer
Winter
NOR
0.5
0.4
0.3
0.2
0.1
0.0
Δ17O (NO3-) (‰)
δ15N (NO3-) (‰)

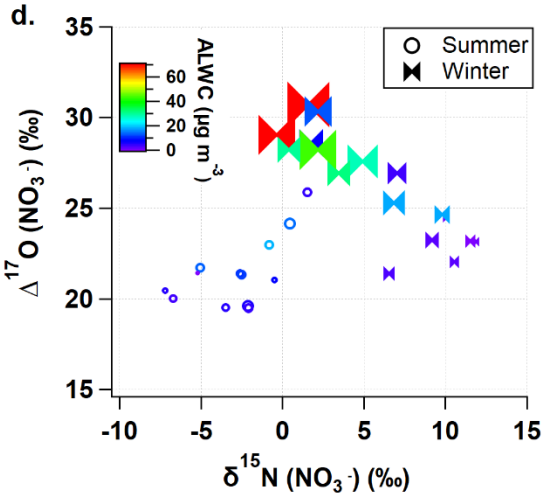
d.
Summer
Winter
ALWC (μg m-3)
60
40
20
0
Δ17O (NO3-) (‰)
δ15N (NO3-) (‰)

611

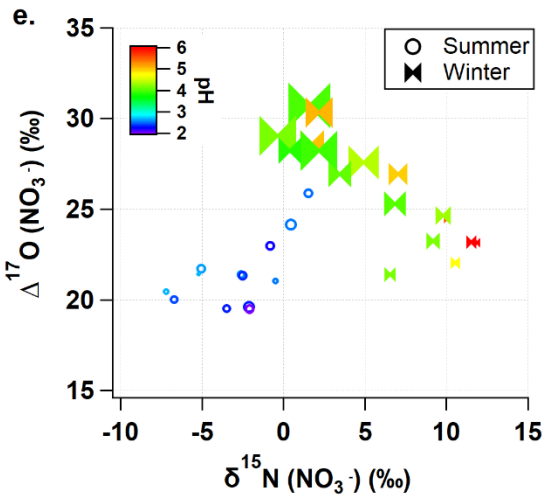
e.
Summer
Winter
pH
6
5
4
3
2
Δ17O (NO3-) (‰)
δ15N (NO3-) (‰)

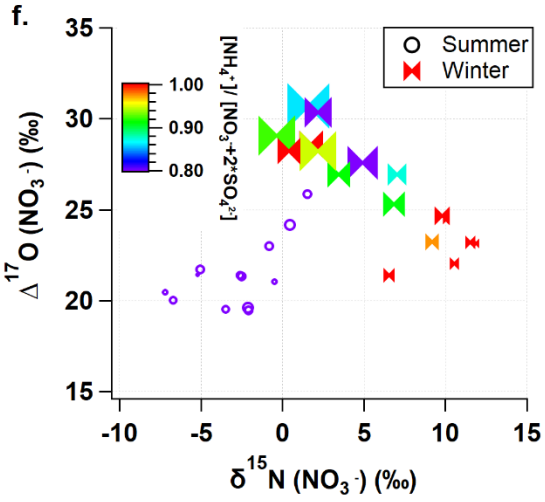
f.
Summer
Winter
[NH4+]/ [NO3-+2*SO4 2-]
1.00
0.90
0.80
Δ17O (NO3-) (‰)
δ15N (NO3-) (‰)

612

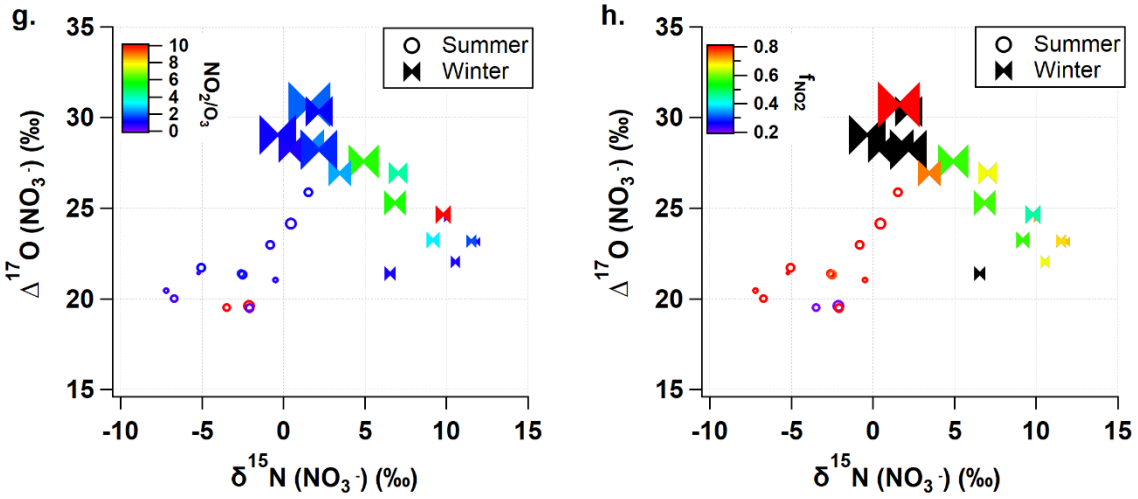

Figure 4. The relationship of measured $\delta^{15}N\ (NO_3^-)$ and $\Delta^{17}O\ (NO_3^-)$ values with key parameters during the summer (open circle) and winter (closed ribbon). The predicted $\Delta^{17}O\ (NO_3^-)$ values are presented as dotted rectangles for the tree major NO_3^- formation pathways (R4, R7, and R8, see Sect. 2.3.2 for details) in (a) summer and (b) winter. Data are color coded by (a) and (b) nitrate concentrations, (c) NOR, (d) ALWC, (e) pH, (f) $[NH_4^+]/([SO_4^{2-}]+[NO_3^-])$ equivalent ratio, (g) NO_2/O_3 ratio, and (h) f_{NO2}. Marker size is proportional to $PM_{2.5}$ concentration ranging from 10 μg m^{-3} to 100 μg m^{-3}.

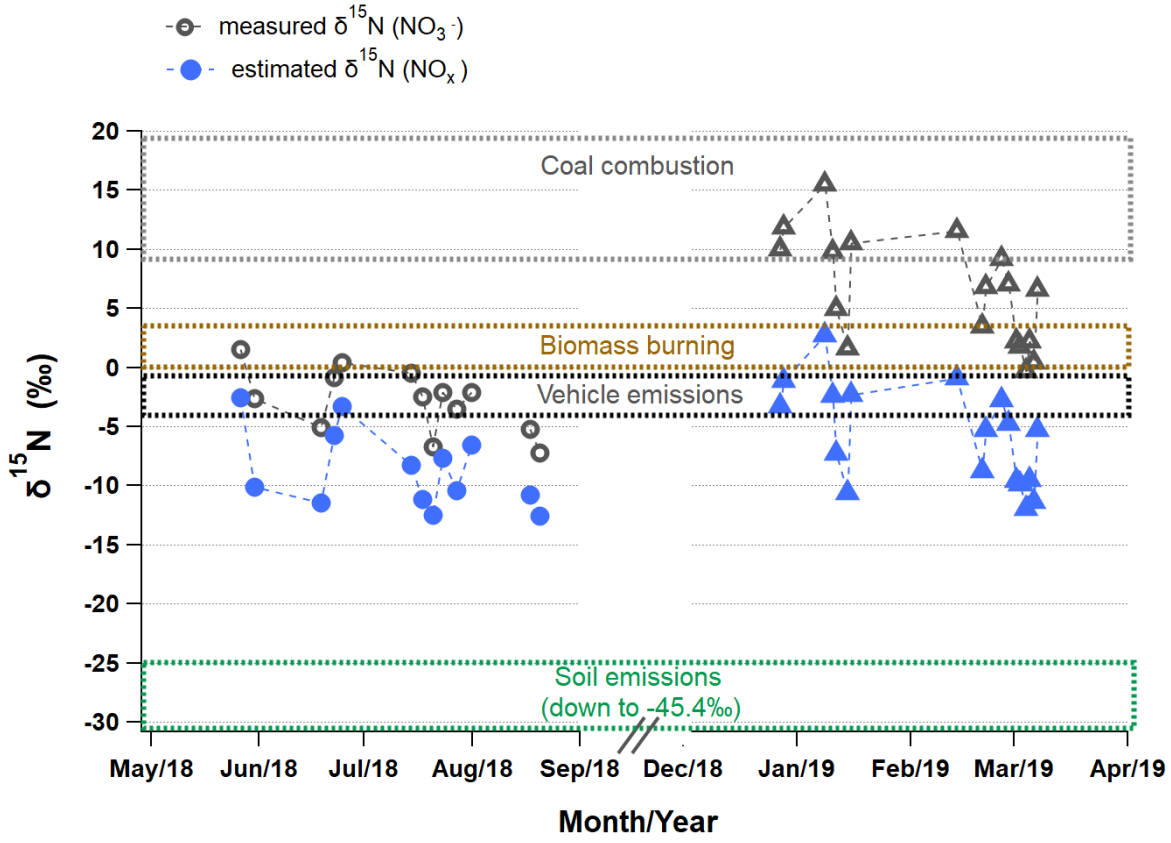

622

623 **Figure 5. Variations in measured $\delta^{15}N$ (NO_3^-) (open) and estimated $\delta^{15}N$ $(NO_x)_{atmosphere}$ (closed) in**
624 **Seoul during the summer (circle) and winter (triangle). The $\delta^{15}N$ (NO_x) range (mean ±**
625 **1sd) of source end members are distinguished by dotted boxes in different colors: coal**
626 **combustion (14.2 ± 4.5 ‰) (Felix et al., 2012; Heaton, 1990), biomass burning (1.8 ±1.8**
627 **‰) (Fibiger and Hastings, 2016), vehicle emissions (-2.5 ± 1.5 ‰) (Walters et al., 2015),**
628 **and biogenic soil emissions (-35.1 ± 10.2 ‰) (Felix and Elliott, 2014; Li and Wang, 2008;**
629 **Yu and Elliott, 2017).**

630

631

References

Alexander, B., Hastings, M. G., Allman, D. J., Dachs, J., Thornton, J. A. and Kunasek, S. A.: Quantifying atmospheric nitrate formation pathways based on a global model of the oxygen isotopic composition (Δ^{17}O) of atmospheric nitrate, Atmos. Chem. Phys., 9(14), 5043–5056, doi:10.5194/acp-9-5043-2009, 2009.

Alexander, B., Sherwen, T., Holmes, C. D., Fisher, J. A., Chen, Q., Evans, M. J. and Kasibhatla, P.: Global inorganic nitrate production mechanisms: comparison of a global model with nitrate isotope observations, Atmos. Chem. Phys., 20(6), 3859–3877, doi:10.5194/acp-20-3859-2020, 2020.

Carslaw, D. C. and Ropkins, K.: openair — An R package for air quality data analysis, Environ. Model. Softw., 27–28, 52–61, doi:10.1016/j.envsoft.2011.09.008, 2012.

Casciotti, K. L., Sigman, D. M., Hastings, M. G., Böhlke, J. K. and Hilkert, A.: Measurement of the oxygen isotopic composition of nitrate in seawater and freshwater using the denitrifier method, Anal. Chem., 74(19), 4905–4912, doi:10.1021/ac020113w, 2002.

Chen, J., Li, C., Ristovski, Z., Milic, A., Gu, Y., Islam, M. S., Wang, S., Hao, J., Zhang, H., He, C., Guo, H., Fu, H., Miljevic, B., Morawska, L., Thai, P., LAM, Y. F., Pereira, G., Ding, A., Huang, X. and Dumka, U. C.: A review of biomass burning: Emissions and impacts on air quality, health and climate in China, Sci. Total Environ., 579(November 2016), 1000–1034, doi:10.1016/j.scitotenv.2016.11.025, 2017.

Cheng, J., Su, J., Cui, T., Li, X., Dong, X., Sun, F., Yang, Y., Tong, D., Zheng, Y., Li, J., Zhang, Q. and He, K.: Dominant role of emission reduction in $PM_{2.5}$ air quality improvement in Beijing during 2013-2017: a model-based decomposition analysis, Atmos. Chem. Phys., 19, 6125–6146, doi:10.5194/acp-19-6125-2019, 2019.

Elliott, E. M., Yu, Z., Cole, A. S. and Coughlin, J. G.: Isotopic advances in understanding reactive nitrogen deposition and atmospheric processing, Sci. Total Environ., 662, 393–403, doi:10.1016/J.SCITOTENV.2018.12.177, 2019.

Felix, J. D. and Elliott, E. M.: Isotopic composition of passively collected nitrogen dioxide emissions: Vehicle, soil and livestock source signatures, Atmos. Environ., 92, 359–366, doi:10.1016/j.atmosenv.2014.04.005, 2014.

Felix, J. D., Elliott, E. M. and Shaw, S. L.: Nitrogen Isotopic Composition of Coal-Fired Power Plant

NO x : Influence of Emission Controls and Implications for Global Emission Inventories, Environ. Sci. Technol., 46(6), 3528–3535, doi:10.1021/es203355v, 2012.

Fibiger, D. L. and Hastings, M. G.: First Measurements of the Nitrogen Isotopic Composition of NO $_x$ from Biomass Burning, Environ. Sci. Technol., 50(21), 11569–11574, doi:10.1021/acs.est.6b03510, 2016.

Fountoukis, C. and Nenes, A.: ISORROPIA II: a computationally efficient thermodynamic equilibrium model for K+- Ca2+-Mg2+-NH+ 4 -Na+-SO2− 4 -NO− 3 -Cl−-H2O aerosols, Atmos. Chem. Phys., 7(17), 4639–4659, doi:10.5194/acp-7-4639-2007, 2007.

Freyer, H. D.: Seasonal variation of 15N/14N ratios in atmospheric nitrate species, Tellus B, 43(1), 30–44, doi:10.1034/j.1600-0889.1991.00003.x, 1991.

Freyer, H. D., Kley, D., Volz-Thomas, A. and Kobel, K.: On the interaction of isotopic exchange processes with photochemical reactions in atmospheric oxides of nitrogen, J. Geophys. Res., 98(D8), 14791, doi:10.1029/93JD00874, 1993.

Goldberg, D. L., Saide, P. E., Lamsal, L. N., de Foy, B., Lu, Z., Woo, J.-H., Kim, Y., Kim, J., Gao, M., Carmichael, G. and Streets, D. G.: A top-down assessment using OMI NO2 suggests an underestimate in the NOx emissions inventory in Seoul, South Korea, during KORUS-AQ, Atmos. Chem. Phys., 19(3), 1801–1818, doi:10.5194/acp-19-1801-2019, 2019.

Guha, T., Lin, C. T., Bhattacharya, S. K., Mahajan, A. S., Ou-Yang, C.-F., Lan, Y.-P., Hsu, S. C. and Liang, M.-C.: Isotopic ratios of nitrate in aerosol samples from Mt. Lulin, a high-altitude station in Central Taiwan, Atmos. Environ., 154, 53–69, doi:10.1016/J.ATMOSENV.2017.01.036, 2017.

Hallquist, M., Stewart, D. J., Stephenson, S. K. and Anthony Cox, R.: Hydrolysis of N2O5 on sub-micron sulfate aerosols, Phys. Chem. Chem. Phys., 5(16), 3453, doi:10.1039/b301827j, 2003.

He, P., Xie, Z., Chi, X., Yu, X., Fan, S., Kang, H., Liu, C. and Zhan, H.: Atmospheric Δ17O(NO3-) reveals nocturnal chemistry dominates nitrate production in Beijing haze, Atmos. Chem. Phys., 18(19), 14465–14476, doi:10.5194/acp-18-14465-2018, 2018.

He, P., Xie, Z., Yu, X., Wang, L., Kang, H. and Yue, F.: The observation of isotopic compositions of atmospheric nitrate in Shanghai China and its implication for reactive nitrogen chemistry, Sci. Total Environ., 714, 136727, doi:10.1016/J.SCITOTENV.2020.136727, 2020.

Heaton, T. H. E.: $^{15}N/^{14}N$ ratios of NOx from vehicle engines and coal-fired power stations, Tellus B, 42(3), 304–307, doi:10.1034/j.1600-0889.1990.00007.x-i1, 1990.

Ishino, S., Hattori, S., Savarino, J., Jourdain, B., Preunkert, S., Legrand, M., Caillon, N., Barbero, A., Kuribayashi, K. and Yoshida, N.: Seasonal variations of triple oxygen isotopic compositions of atmospheric sulfate, nitrate, and ozone at Dumont d'Urville, coastal Antarctica, Atmos. Chem. Phys., 17(5), 3713–3727, doi:10.5194/ACP-17-3713-2017, 2017.

Kaiser, J., Hastings, M. G., Houlton, B. Z., Röckmann, T. and Sigman, D. M.: Triple oxygen isotope analysis of nitrate using the denitrifier method and thermal decomposition of N2O, Anal. Chem., 79(2), 599–607, doi:10.1021/ac061022s, 2007.

Kamezaki, K., Hattori, S., Iwamoto, Y., Ishino, S., Furutani, H., Miki, Y., Uematsu, M., Miura, K. and Yoshida, N.: Tracing the sources and formation pathways of atmospheric particulate nitrate over the Pacific Ocean using stable isotopes, Atmos. Environ., 209, 152–166, doi:10.1016/J.ATMOSENV.2019.04.026, 2019.

Kang, H., Zhu, B., Gao, J., He, Y., Wang, H., Su, J., Pan, C., Zhu, T. and Yu, B.: Potential impacts of cold frontal passage on air quality over the Yangtze River Delta, China, Atmos. Chem. Phys., 19(6), 3673–3685, doi:10.5194/acp-19-3673-2019, 2019.

Kim, H., Zhang, Q. and Sun, Y.: Measurement report: Characterization of severe spring haze episodes and influences of long-range transport in the Seoul metropolitan area in March 2019, Atmos. Chem. Phys., 20(19), 11527–11550, doi:10.5194/acp-20-11527-2020, 2020a.

Kim, H. C., Kim, S., Lee, S.-H., Kim, B.-U. and Lee, P.: Fine-Scale Columnar and Surface NOx Concentrations over South Korea: Comparison of Surface Monitors, TROPOMI, CMAQ and CAPSS Inventory, Atmosphere (Basel)., 11(1), 101, doi:10.3390/atmos11010101, 2020b.

Kim, S.-W., Yoon, S.-C., Kim, J. and Kim, S.-Y.: Seasonal and monthly variations of columnar aerosol optical properties over east Asia determined from multi-year MODIS, LIDAR, and AERONET Sun/sky radiometer measurements, Atmos. Environ., 41(8), 1634–1651, doi:10.1016/j.atmosenv.2006.10.044, 2007.

Lee, H.-J., Jo, H.-Y., Kim, S.-W., Park, M.-S. and Kim, C.-H.: Impacts of atmospheric vertical structures on transboundary aerosol transport from China to South Korea, Sci. Rep., 9(1), 13040, doi:10.1038/s41598-019-49691-z, 2019.

718 Lelieveld, J., Evans, J. S., Fnais, M., Giannadaki, D. and Pozzer, A.: The contribution of outdoor air
719 pollution sources to premature mortality on a global scale, Nature, 525(7569), 367–371,
720 doi:10.1038/nature15371, 2015.

721 Li, D. and Wang, X.: Nitrogen isotopic signature of soil-released nitric oxide (NO) after fertilizer
722 application, Atmos. Environ., 42(19), 4747–4754, doi:10.1016/j.atmosenv.2008.01.042, 2008.

723 Li, H., Zhang, Q., Zheng, B., Chen, C., Wu, N., Guo, H., Zhang, Y., Zheng, Y., Li, X. and He, K.:
724 Nitrate-driven urban haze pollution during summertime over the North China Plain, Atmos. Chem.
725 Phys., 18(8), 5293–5306, doi:10.5194/acp-18-5293-2018, 2018.

726 Li, J., Zhang, X., Orlando, J., Tyndall, G. and Michalski, G.: Quantifying the nitrogen isotope effects
727 during photochemical equilibrium between NO and NO2: Implications for δ15N in tropospheric
728 reactive nitrogen, Atmos. Chem. Phys., 20(16), 9805–9819, doi:10.5194/acp-20-9805-2020, 2020.

729 Li, J., Davy, P., Harvey, M., Katzman, T., Mitchell, T. and Michalski, G.: Nitrogen isotopes in nitrate
730 aerosols collected in the remote marine boundary layer: Implications for nitrogen isotopic
731 fractionations among atmospheric reactive nitrogen species, Atmos. Environ., 245, 118028,
732 doi:10.1016/j.atmosenv.2020.118028, 2021.

733 Li, Z., Walters, W. W., Hastings, M. G., Zhang, Y., Song, L., Liu, D., Zhang, W., Pan, Y., Fu, P. and
734 Fang, Y.: Nitrate Isotopic Composition in Precipitation at a Chinese Megacity: Seasonal Variations,
735 Atmospheric Processes, and Implications for Sources, Earth Sp. Sci., 6(11), 2200–2213,
736 doi:10.1029/2019EA000759, 2019.

737 Lim, S., Lee, M., Czimczik, C. I., Joo, T., Holden, S., Mouteva, G., Santos, G. M., Xu, X., Walker, J.,
738 Kim, S., Kim, H. S., Kim, S. and Lee, S.: Source signatures from combined isotopic analyses of $PM_{2.5}$
739 carbonaceous and nitrogen aerosols at the peri-urban Taehwa Research Forest, South Korea in
740 summer and fall, Sci. Total Environ., 655, 1505–1514, doi:10.1016/j.scitotenv.2018.11.157, 2019.

741 Lim, S., Yang, X., Lee, M., Li, G., Gao, Y., Shang, X., Zhang, K., Czimczik, C. I., Xu, X., Bae, M.-
742 S., Moon, K.-J. and Jeon, K.: Fossil-driven secondary inorganic $PM_{2.5}$ enhancement in the North
743 China Plain: Evidence from carbon and nitrogen isotopes, Environ. Pollut., 266, 115163,
744 doi:10.1016/J.ENVPOL.2020.115163, 2020.

745 Liu, Z., Gao, W., Yu, Y., Hu, B., Xin, J., Sun, Y., Wang, L., Wang, G., Bi, X., Zhang, G., Xu, H.,
746 Cong, Z., He, J., Xu, J. and Wang, Y.: Characteristics of $PM_{2.5}$ mass concentrations and chemical

747 species in urban and background areas of China: emerging results from the CARE-China network,
748 Atmos. Chem. Phys., 18(12), 8849–8871, doi:10.5194/acp-18-8849-2018, 2018.

749 McIlvin, M. R. and Casciotti, K. L.: Technical updates to the bacterial method for nitrate isotopic
750 analyses, Anal. Chem., 83(5), 1850–1856, doi:10.1021/AC1028984, 2011.

751 Michalski, G. and Bhattacharya, S. K.: The role of symmetry in the mass independent isotope effect in
752 ozone, Proc. Natl. Acad. Sci., 106(14), 5493–5496, doi:10.1073/PNAS.0812755106, 2009.

753 Michalski, G., Scott, Z., Kabiling, M. and Thiemens, M. H.: First measurements and modeling of Δ^{17}
754 O in atmospheric nitrate, Geophys. Res. Lett., 30(16), doi:10.1029/2003GL017015, 2003.

755 Michalski, G., Meixner, T., Fenn, M., Hernandez, L., Sirulnik, A., Edith Allen, A. and Thiemens†,
756 M.: Tracing Atmospheric Nitrate Deposition in a Complex Semiarid Ecosystem Using Δ17O, ,
757 doi:10.1021/ES034980+, 2004.

758 Morin, S., Savarino, J., Frey, M. M., Domine, F., Jacobi, H.-W., Kaleschke, L. and Martins, J. M. F.:
759 Comprehensive isotopic composition of atmospheric nitrate in the Atlantic Ocean boundary layer
760 from 65°S to 79°N, J. Geophys. Res., 114(D5), D05303, doi:10.1029/2008JD010696, 2009.

761 Morin, S., Sander, R. and Savarino, J.: Simulation of the diurnal variations of the oxygen isotope
762 anomaly (Δ 17 O) of reactive atmospheric species, Atmos. Chem. Phys., 11(8), 3653–3671,
763 doi:10.5194/acp-11-3653-2011, 2011.

764 Nelson, D. M., Tsunogai, U., Ding, D., Ohyama, T., Komatsu, D. D., Nakagawa, F., Noguchi, I. and
765 Yamaguchi, T.: Triple oxygen isotopes indicate urbanization affects sources of nitrate in wet and dry
766 atmospheric deposition, Atmos. Chem. Phys., 18(9), 6381–6392, doi:10.5194/acp-18-6381-2018,
767 2018.

768 Park, Y., Park, K., Kim, H., Yu, S., Noh, S., Kim, M., Kim, J., Ahn, J., Lee, M., Seok, K. and Kim,
769 Y.: Characterizing isotopic compositions of TC-C, NO_3^--N, and NH_4^+-N in $PM_{2.5}$ in South Korea:
770 Impact of China's winter heating, Environ. Pollut., 233, 735–744,
771 doi:10.1016/J.ENVPOL.2017.10.072, 2018.

772 Parnell, A. C., Inger, R., Bearhop, S. and Jackson, A. L.: Source Partitioning Using Stable Isotopes:
773 Coping with Too Much Variation, edited by S. Rands, PLoS One, 5(3), e9672,
774 doi:10.1371/journal.pone.0009672, 2010.

Parnell, A. C., Phillips, D. L., Bearhop, S., Semmens, B. X., Ward, E. J., Moore, J. W., Jackson, A. L., Grey, J., Kelly, D. J. and Inger, R.: Bayesian stable isotope mixing models, Environmetrics, 24(6), 387–399, doi:10.1002/env.2221, 2013.

Quan, J., Dou, Y., Zhao, X., Liu, Q., Sun, Z., Pan, Y., Jia, X., Cheng, Z., Ma, P., Su, J., Xin, J. and Liu, Y.: Regional atmospheric pollutant transport mechanisms over the North China Plain driven by topography and planetary boundary layer processes, Atmos. Environ., 221, 117098, doi:10.1016/J.ATMOSENV.2019.117098, 2020.

Rose, L. A., Yu, Z., Bain, D. J. and Elliott, E. M.: High resolution, extreme isotopic variability of precipitation nitrate, Atmos. Environ., 207, 63–74, doi:10.1016/J.ATMOSENV.2019.03.012, 2019.

Saunders, S. M., Jenkin, M. E., Derwent, R. G. and Pilling, M. J.: Protocol for the development of the Master Chemical Mechanism, MCM v3 (Part A): Tropospheric degradation of non-aromatic volatile organic compounds, Atmos. Chem. Phys., 3(1), 161–180, doi:10.5194/acp-3-161-2003, 2003.

Savarino, J., Kaiser, J., Morin, S., Sigman, D. M. and Thiemens, M. H.: Nitrogen and oxygen isotopic constraints on the origin of atmospheric nitrate in coastal Antarctica, Atmos. Chem. Phys., 7(8), 1925–1945, doi:10.5194/acp-7-1925-2007, 2007.

Savarino, J., Morin, S., Erbland, J., Grannec, F., Patey, M. D., Vicars, W., Alexander, B. and Achterberg, E. P.: Isotopic composition of atmospheric nitrate in a tropical marine boundary layer., Proc. Natl. Acad. Sci. U. S. A., 110(44), 17668–73, doi:10.1073/pnas.1216639110, 2013.

Shao, P., Tian, H., Sun, Y., Liu, H., Wu, B., Liu, S., Liu, X., Wu, Y., Liang, W., Wang, Y., Gao, J., Xue, Y., Bai, X., Liu, W., Lin, S. and Hu, G.: Characterizing remarkable changes of severe haze events and chemical compositions in multi-size airborne particles (PM_1, $PM_{2.5}$ and PM_{10}) from January 2013 to 2016–2017 winter in Beijing, China, Atmos. Environ., 189, 133–144, doi:10.1016/J.ATMOSENV.2018.06.038, 2018.

Sharma, H. D., Jervis, R. E. and Wong, K. Y.: Isotopic exchange reactions in nitrogen oxides, J. Phys. Chem., 74(4), 923–933, doi:10.1021/j100699a044, 1970.

Shi, C., Nduka, I. C., Yang, Y., Huang, Y., Yao, R., Zhang, H., He, B., Xie, C., Wang, Z. and Yim, S. H. L.: Characteristics and meteorological mechanisms of transboundary air pollution in a persistent heavy $PM_{2.5}$ pollution episode in Central-East China, Atmos. Environ., 223, 117239, doi:10.1016/J.ATMOSENV.2019.117239, 2020.

Song, W., Wang, Y.-L., Yang, W., Sun, X.-C., Tong, Y.-D., Wang, X.-M., Liu, C.-Q., Bai, Z.-P. and Liu, X.-Y.: Isotopic evaluation on relative contributions of major NOx sources to nitrate of $PM_{2.5}$ in Beijing, Environ. Pollut., 248, 183–190, doi:10.1016/J.ENVPOL.2019.01.081, 2019.

Song, W., Liu, X.-Y., Wang, Y.-L., Tong, Y.-D., Bai, Z.-P. and Liu, C.-Q.: Nitrogen isotope differences between atmospheric nitrate and corresponding nitrogen oxides: A new constraint using oxygen isotopes, Sci. Total Environ., 701, 134515, doi:10.1016/J.SCITOTENV.2019.134515, 2020.

Stein, A. F., Draxler, R. R., Rolph, G. D., Stunder, B. J. B., Cohen, M. D. and Ngan, F.: NOAA's HYSPLIT Atmospheric Transport and Dispersion Modeling System, Bull. Am. Meteorol. Soc., 96(12), 2059–2077, doi:10.1175/BAMS-D-14-00110.1, 2015.

Thiemens, M. H.: Mass-independent isotope effects in planetary atmospheres and the early solar system, Science (80-.)., 283(5400), 341–345, doi:10.1126/science.283.5400.341, 1999.

Thiemens, M. H.: HISTORY AND APPLICATIONS OF MASS-INDEPENDENT ISOTOPE EFFECTS, Annu. Rev. Earth Planet. Sci., 34(1), 217–262, doi:10.1146/annurev.earth.34.031405.125026, 2006.

Tong, D., Zhang, Q., Liu, F., Geng, G., Zheng, Y., Xue, T., Hong, C., Wu, R., Qin, Y., Zhao, H., Yan, L. and He, K.: Current Emissions and Future Mitigation Pathways of Coal-Fired Power Plants in China from 2010 to 2030, Environ. Sci. Technol., 52(21), 12905–12914, doi:10.1021/acs.est.8b02919, 2018.

Vicars, W. C. and Savarino, J.: Quantitative constraints on the ^{17}O-excess (Δ^{17}O) signature of surface ozone: Ambient measurements from 50°N to 50°S using the nitrite-coated filter technique, Geochim. Cosmochim. Acta, 135, 270–287, doi:10.1016/J.GCA.2014.03.023, 2014.

Vicars, W. C., Bhattacharya, S. K., Erbland, J. and Savarino, J.: Measurement of the ^{17}O-excess (Δ^{17}O) of tropospheric ozone using a nitrite-coated filter, Rapid Commun. Mass Spectrom., 26(10), 1219–1231, doi:10.1002/rcm.6218, 2012.

Wahner, A., Mentel, T. F., Sohn, M. and Stier, J.: Heterogeneous reaction of N_2O_5 on sodium nitrate aerosol, J. Geophys. Res. Atmos., 103(D23), 31103–31112, doi:10.1029/1998JD100022, 1998.

Walters, W. W. and Michalski, G.: Theoretical calculation of nitrogen isotope equilibrium exchange fractionation factors for various NO_y molecules, Geochim. Cosmochim. Acta, 164, 284–297, doi:10.1016/J.GCA.2015.05.029, 2015.

Walters, W. W. and Michalski, G.: Theoretical calculation of oxygen equilibrium isotope fractionation factors involving various NO molecules, OH, and H_2O and its implications for isotope variations in atmospheric nitrate, Geochim. Cosmochim. Acta, 191, 89–101, doi:10.1016/j.gca.2016.06.039, 2016.

Walters, W. W., Goodwin, S. R. and Michalski, G.: Nitrogen Stable Isotope Composition ($\delta^{15}N$) of Vehicle-Emitted NO_x, Environ. Sci. Technol., 49(4), 2278–2285, doi:10.1021/es505580v, 2015.

Walters, W. W., Simonini, D. S. and Michalski, G.: Nitrogen isotope exchange between NO and NO_2 and its implications for $\delta^{15}N$ variations in tropospheric NO_x and atmospheric nitrate, Geophys. Res. Lett., 43(1), 440–448, doi:10.1002/2015GL066438, 2016.

Walters, W. W., Fang, H. and Michalski, G.: Summertime diurnal variations in the isotopic composition of atmospheric nitrogen dioxide at a small midwestern United States city, Atmos. Environ., 179, 1–11, doi:10.1016/J.ATMOSENV.2018.01.047, 2018.

Wang, Y., Wang, Y., Wang, L., Petäjä, T., Zha, Q., Gong, C., Li, S., Pan, Y., Hu, B., Xin, J. and Kulmala, M.: Increased inorganic aerosol fraction contributes to air pollution and haze in China, Atmos. Chem. Phys., 19(9), 5881–5888, doi:10.5194/acp-19-5881-2019, 2019a.

Wang, Y., Song, W., Yang, W., Sun, X., Tong, Y., Wang, X., Liu, C., Bai, Z. and Liu, X.: Influences of Atmospheric Pollution on the Contributions of Major Oxidation Pathways to PM $_{2.5}$ Nitrate Formation in Beijing, J. Geophys. Res. Atmos., 124(7), 4174–4185, doi:10.1029/2019JD030284, 2019b.

van der Werf, G. R., Randerson, J. T., Giglio, L., Collatz, G. J., Mu, M., Kasibhatla, P. S., Morton, D. C., DeFries, R. S., Jin, Y. and van Leeuwen, T. T.: Global fire emissions and the contribution of deforestation, savanna, forest, agricultural, and peat fires (1997–2009), Atmos. Chem. Phys., 10(23), 11707–11735, doi:10.5194/acp-10-11707-2010, 2010.

Xie, Y., Dai, H., Zhang, Y., Wu, Y., Hanaoka, T. and Masui, T.: Comparison of health and economic impacts of $PM_{2.5}$ and ozone pollution in China, Environ. Int., 130, 104881, doi:10.1016/J.ENVINT.2019.05.075, 2019.

Xu, W., Sun, Y., Wang, Q., Zhao, J., Wang, J., Ge, X., Xie, C., Zhou, W., Du, W., Li, J., Fu, P., Wang, Z., Worsnop, D. R. and Coe, H.: Changes in Aerosol Chemistry From 2014 to 2016 in Winter in Beijing: Insights From High-Resolution Aerosol Mass Spectrometry, J. Geophys. Res. Atmos.,

124(2), 1132–1147, doi:10.1029/2018JD029245, 2019.

Yu, Z. and Elliott, E. M.: Novel method for nitrogen isotopic analysis of soil-emitted nitric oxide, Environ. Sci. Technol., 51(11), 6268–6278, doi:10.1021/acs.est.7b00592, 2017.

Zhao, H., Zhang, X., Zhang, S., Chen, W., Tong, D., Xiu, A., Zhao, H., Zhang, X., Zhang, S., Chen, W., Tong, D. Q. and Xiu, A.: Effects of Agricultural Biomass Burning on Regional Haze in China: A Review, Atmosphere (Basel)., 8(12), 88, doi:10.3390/atmos8050088, 2017.

Zheng, H., Kong, S., Wu, F., Cheng, Y., Niu, Z., Zheng, S., Yang, G., Yao, L., Yan, Q., Wu, J., Zheng, M., Chen, N., Xu, K., Yan, Y., Liu, D., Zhao, D., Zhao, T., Bai, Y., Li, S. and Qi, S.: Intra-regional transport of black carbon between the south edge of the North China Plain and central China during winter haze episodes, Atmos. Chem. Phys., 19(7), 4499–4516, doi:10.5194/acp-19-4499-2019, 2019.

Zong, Z., Wang, X., Tian, C., Chen, Y., Fang, Y., Zhang, F., Li, C., Sun, J., Li, J. and Zhang, G.: First assessment of NO_x sources at a regional background site in north China using isotopic analysis linked with modeling, Environ. Sci. Technol., 51(11), 5923–5931, doi:10.1021/acs.est.6b06316, 2017.

Zong, Z., Tan, Y., Wang, X., Tian, C., Li, J., Fang, Y., Chen, Y., Cui, S. and Zhang, G.: Dual-modelling-based source apportionment of NOx in five Chinese megacities: Providing the isotopic footprint from 2013 to 2014, Environ. Int., 137, 105592, doi:10.1016/J.ENVINT.2020.105592, 2020.